nature genetics

Article

https://doi.org/10.1038/s41588-025-02415-8

JMJD2 regulates enhancer–promoter interactions via biomolecular condensate formation

Received: 13 June 2024

Accepted: 17 October 2025

Published online: 16 December 2025

Check for updates

Shaoshuai Jiang[1,2,3,4,13], Xinyi Liu[1,2,3,4,13], Zhuheng Zhang[1,2,3,4,13], Mingzhu Yang[1,5,13], Xing Zhu[1], Lin Ma[1], Longying Zhao[1], Xiaoru Ling[1], Ziqiang Zhou[1,6], Ziqiang Wu[1], Jiale Qu[1], Haochen Li[1], Jiawei Liang[6], Zhiheng Deng[6], Qi Tian[1], Xiaona Huang[1], Xianglin Huang[1], Jin Tan[1], Jun Sun[1,3], Jia Wang[7], Diana Guallar[8], Partha Pratim Das[9], Luca Pinello[10], Liang Wang[11], Hongfu Wu[2], Dong-feng Huang[1], Jichang Wang[1], Hancheng Lin[1], Jin Bai[2] ✉, Lili Fan[12] ✉, Wei Chi[4] ✉, Xue Xiao[3] ✉ & Junjun Ding[1,2,3,4] ✉

Enhancer–promoter (E-P) interactions regulate transcription during cell fate determination. However, the regulatory mechanisms underlying E-P interactions have remained elusive. Here we present a chromatin-interaction-based proteomic approach, LoopID, to profile proteins (termed the looposome) at certain E-P anchors. We find that histone demethylase JMJD2, a key looposome component, can regulate E-P interactions and the looposome in a catalytic-independent manner through formation of biomolecular condensates. Furthermore, we introduce a system to engineer E-P interactions by assembling JMJD2 condensates at certain genomic loci, enabling construction of cell-type-specific E-P interactions to promote cellular reprogramming into pluripotent or two-cell-like cells. Our findings reveal a noncanonical function of a histone demethylase in regulation of chromatin organization and provide a strategy to regulate cell fate transitions through E-P interactions.

Cell-type-specific gene expression programs in mammalian cells are generally orchestrated by *cis*-regulatory elements called enhancers[1]. In particular, super-enhancers (SEs) are crucial for regulation of genes related to cell fate decisions[2]. Enhancers connect to their cognate promoters through chromatin interactions to regulate gene transcription[3], and aberrant enhancer–promoter (E-P) interactions can result in gene dysregulation, forming the mechanistic basis of various diseases and developmental disorders[4]. Thus, it is crucial to explore the regulatory mechanisms of E-P interactions.

E-P interactions—specifically, SE–promoter interactions—are occupied by multiple proteins[5], including transcription factors[6], transcriptional coactivators[7] and E-P structural regulator YY1[8,9]. These proteins, which form multimolecular assemblies at chromatin interactions, are termed the 'looposome' in this study. There is evidence that proteins in the looposome can drive chromatin looping[10]. However, the protein components of the looposome at E-P interactions remain to be systematically profiled.

Here we developed LoopID, a chromatin-interaction-based proteomic approach to identify looposome proteins and found that the histone demethylase JMJD2 could mediate E-P interactions in a catalytic-independent manner through formation of biomolecular condensates. Specifically, JMJD2 condensates maintain pluripotent E-P interactions in mouse embryonic stem cells (ES cells) and promote two-cell-specific E-P interactions upon overexpression, both independently of its catalytic activity. Based on this mechanism, we engineered cell-type-specific E-P interactions by assembling JMJD2 condensates

A full list of affiliations appears at the end of the paper. ✉e-mail: bj@xzhmu.edu.cn; fanlili@jnu.edu.cn; chiwei@mail.sysu.edu.cn; xiaoxuela@scu.edu.cn; dingjunj@mail.sysu.edu.cn

at specific genomic loci. This approach facilitates cellular reprogramming into pluripotent cells or two-cell-like cells (2CLCs), providing a strategy for regulation of cell fate transition through E-P interactions.

Results

Establishment of LoopID to identify looposome

To identify looposome proteins (Fig. 1a), we developed LoopID, a chromatin-interaction-based proteomic approach, through integration of CRISPR–dCas9 technology and split proximity labeling enzyme split-TurboID[11]. The latter consists of two TurboID fragments, comprising the amino-terminal split-TurboID(N) and the carboxy-terminal split-TurboID(C), which can be brought together within approximately 35 nm (ref. 11) to reconstitute an active enzyme to proximately biotinylate proteins. Split-TurboID(N) and split-TurboID(C) were tethered to certain chromatin interactions by *Streptococcus pyogenes* dCas9 (SpdCas9) and *Staphylococcus aureus* dCas9 (SadCas9), respectively, using single-guide RNA (sgRNA) pairs (Fig. 1b and Supplementary Fig. 1a). Once the chromatin had been folded, split-TurboID(N) and split-TurboID(C) were fused together to reconstitute an active TurboID enzyme that effectively biotinylated the proteins at the targeted chromatin interaction (Fig. 1b and Supplementary Fig. 1b,c), as demonstrated by the activation of the enzyme after de novo construction of chromatin interactions (Supplementary Fig. 1d,e). Subsequently, the biotinylated proteins could be identified by streptavidin immunoprecipitation followed by mass spectrometry analysis (Fig. 1b). Thus, LoopID can be used to identify chromatin-interaction-based proteomes.

Using LoopID, we identified the proteins at the SE–promoter interaction of *Nanog* and the E-P interaction of *Oct4* (*Pou5f1*) in mouse ES cells (Fig. 1c), given that both of these genes are essential for pluripotency maintenance[12,13]. We selected the targeted enhancers based on their strong interactions with the target genes, as demonstrated by histone H3 K27 acetylation (H3K27ac) HiChIP[14], their activity according to self-transcribing active regulatory region sequencing (STARR-seq)[15], and their relatively great linear distance from the target promoter to reduce the probability of nonspecific interactions[16] (Fig. 1c). All LoopID constructs and sgRNAs were stably transfected into the cells, and a monoclonal cell line was selected (Supplementary Fig. 1f), ensuring stable expression across multiple cell passages (Supplementary Fig. 1g,h). Chromatin immunoprecipitation followed by sequencing (ChIP–seq) was used to confirm that SadCas9 and SpdCas9 specifically bound the *Nanog* and *Oct4* E-P anchors, either coexpressed (Fig. 1c and Supplementary Fig. 1i) or expressed individually (Supplementary Fig. 1j), and the sgRNAs exhibited effective on-target activity with minimal off-target effects (Supplementary Table 1). The E-P interaction brought SadCas9 and SpdCas9 to interact with each other and reconstituted split-TurboID into an active enzyme (Fig. 1d,e and Supplementary Fig. 1k), with a reconstitution efficiency compatible with spatial proximity-based expectations of E-P interactions (Supplementary Fig. 1l), and this process had minimal effects on the target E-P interactions (Supplementary Fig. 1m). Moreover, the results of streptavidin immunofluorescence (IF) assays confirmed that the active enzymes were located inside the nucleus (Supplementary Fig. 1n). LoopID demonstrated high repeatability among biological replicates (Supplementary Fig. 1o) and was used to identify proteins based on rigorous criteria (false discovery rate (FDR) = 0 (average posterior probability of true protein interaction (AvgP) = 1)[17], fold change (FC) ≥ 3 and count ≥ 30 in both +sgRNA replicates; Supplementary Fig. 1p,q). To further confirm that the LoopID system only effectively labeled proteins at interacting E-P pairs, negative controls were introduced; this showed that LoopID identified more than 20 times more proteins at *Nanog* or *Oct4* E-P interactions compared to sites with low interaction frequencies (Supplementary Fig. 1r). In addition, LoopID activity declined during mitosis, when chromatin becomes highly condensed and E-P interactions are substantially reduced, and increased during G1 phase, when chromatin is more open and E-P interactions are more frequent (Supplementary Fig. 1s). To compare LoopID with regular TurboID[18], we expressed a nonsplit TurboID fused with SpdCas9 to identify proximal proteomes at both the *Oct4* enhancer and promoter regions. LoopID showed significant enrichment of structural factors (CTCF, SMC1A, SMC3) compared to nonsplit TurboID (Supplementary Fig. 1t), demonstrating the superiority of LoopID in detection of E-P interaction proteins. Moreover, expression of SpdCas9–nonsplit TurboID without sgRNA enabled background subtraction from the reconstituted split-TurboID that was initially reconstituted at targeted E-P loci but then dissociated owing to binding turnover (Supplementary Fig. 1u). These results provide support for the specificity and reliability of LoopID in identifying the looposome at the targeted interacting E-P pairs.

The identified looposome contained known chromatin structural regulators including CTCF, cohesin and YY1 (Fig. 1f), reported enhancer- or promoter-binding proteins identified by published H3K27ac or H3K4me3 ChIP–MS[19] or ChIP–seq[20] (Fig. 1f, denoted as 'Known'), and proteins related to transcription (Fig. 1g and Supplementary Table 2). Shortened biotin labeling inefficiently captured these known E-P regulators (Supplementary Fig. 1v). These components were validated by published ChIP–seq and HiChIP experiments (Supplementary Fig. 1w), and the reproducibility of the results was confirmed by LoopID in independent ES cell lines (Supplementary Fig. 1x)

Fig. 1 | Establishment of LoopID to identify looposome proteins. a, Schematic showing the definition of the looposome: the protein components at interacting chromatin loci. **b**, Schematic of LoopID. Two inactive fragments of TurboID (split-TurboID(N) and split-TurboID(C)) were guided by Flag-SpdCas9 and HA-SadCas9, respectively, to target the anchors of chromatin interaction (detailed components of the LoopID system are illustrated in Supplementary Fig. 1a). **c**, Genome browser view showing the two targeted E-P interactions and the specific binding of dCas9. The enhancers and promoters were obtained from published ChIP–seq data for H3K27ac and H3K4me3, respectively[50], and the enhancer activity from published STARR-seq data[15]. The E-P interactions were identified from published H3K27ac HiChIP data[14] (gray arcs). The *y*-axis values represent reads per kilobase million mapped reads (RPKM) for ChIP–seq of histone modifications and CTCF[50], the empirical Bayes shrunken enrichment over input for STARR-seq, and counts per million (CPM) mapped reads for ChIP–seq of dCas9. **d**,**e**, For the *Nanog* E–P interaction (**d**) and the *Oct4* E–P interaction (**e**); left: coimmunoprecipitation confirmed the interaction of the HA-SadCas9–Split-TurboID(C) and Flag-SpdCas9–Split-TurboID(N) proteins in the presence or absence of sgRNAs at the indicated E-P interaction. Right: streptavidin (SA) western blotting results showing biotinylation activity of LoopID in the presence or absence of sgRNAs. 'C + N' refers to cell lines with both ends of LoopID, whereas 'C' refers to cell lines with only the C-terminal fragment, and 'N' refers to cell lines with only the N-terminal fragment (details are illustrated in Supplementary Fig. 1b). Tubulin was used as a loading control. **f**, Core looposome factors were defined as factors common to both the *Nanog* E-P looposome and the *Oct4* E-P looposome (identified by LoopID in three independent ES cell lines and detected by the switched LoopID in *Jmjd2*$^{fl/fl}$ ES cells). Looposome factors were identified by comparing +sgRNA with −sgRNA ($n = 2$ for +sgRNA, $n = 4$ or $n = 3$ for −sgRNA). Circles represent novel factors present at enhancers or promoters, whereas triangles represent known factors identified by public H3K27ac or H3K4me3 ChIP–MS[19] or ChIP–seq[20]. The sizes of the dots represent the average counts of peptides from replicates: two replicates for the *Nanog* E-P looposome, six replicates for the *Oct4* E-P looposome (across three independent ES cell lines) and two replicates for the *Oct4* E-P looposome detected using the switched LoopID. Some known structural regulators are annotated (SMC1A and SMC3 are core components of the cohesin complex, whereas WAPL acts as its release factor). Details and further classification are provided in Supplementary Table 2. **g**, Classification of the core looposome factors. Lists of ERs, transcription factors and cofactors were obtained from published studies[51,52]. The other annotations were based on the PANTHER Protein Class (https://www.pantherdb.org/). Thirty-two 'unclassified' proteins were not included (details in Supplementary Table 2). IB, immunoblotting; IP, immunoprecipitation; IP–MS, immunoprecipitation coupled with mass spectrometry; SA, streptavidin.

https://doi.org/10.1038/s41588-025-02415-8

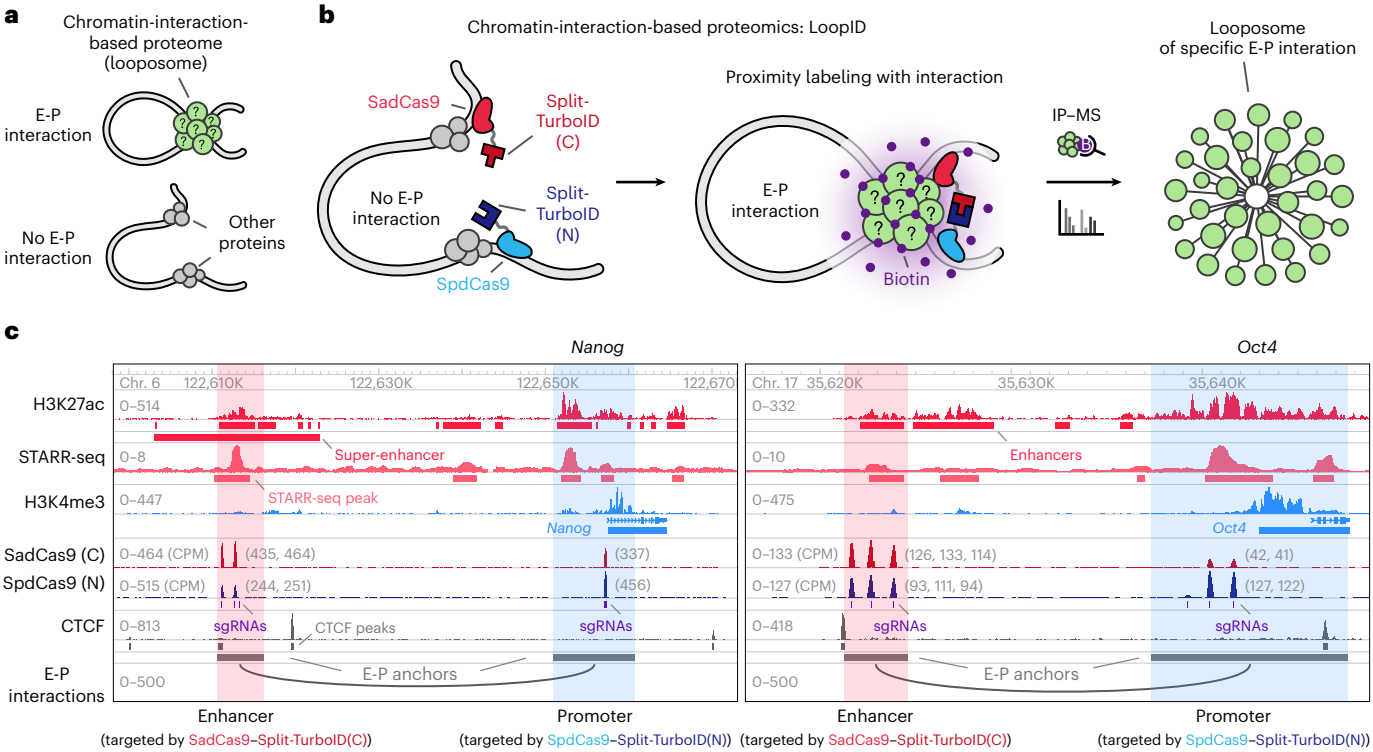

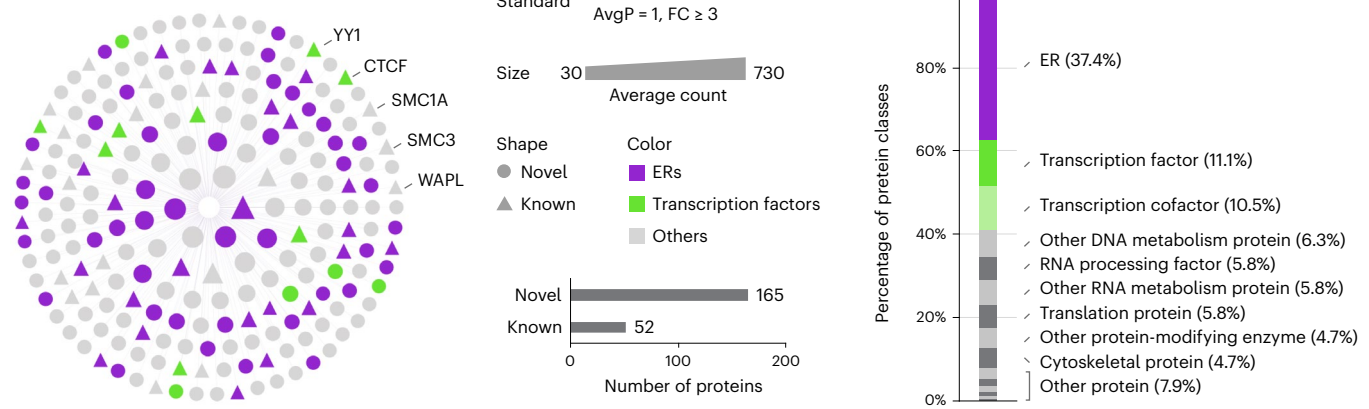

or by swapping the C and N fragments of LoopID (switched LoopID) (Supplementary Fig. 1y), further validating the robustness of LoopID. We also established a core looposome list by integrating LoopID results from different strategies (Supplementary Table 2). Notably, several unknown factors were also enriched in the E-P looposome, which may contain unknown chromatin-structure-regulating proteins (Fig. 1f,g and Supplementary Table 2). Furthermore, looposome factors are composed of abundant epigenetic regulators (ERs) (Fig. 1f,g) and are enriched in pathways or molecular functions related to epigenetic regulation (Supplementary Fig. 1z); however, the roles of ERs in regulating chromatin structures have not been studied extensively.

Looposome factor JMJD2 maintains E-P interactions

ERs are highly enriched in the looposome (Fig. 1f,g), suggesting a potential role in regulation of E-P interactions (Fig. 2a). We evaluated the enrichment of ERs within the looposome at genome-wide E-P anchors based on published ChIP–seq datasets (Fig. 2b) and found that JMJD2 histone demethylases[21] were among the top enriched proteins (Fig. 2c and Supplementary Note 1).

As JMJD2 was observed to be widely located at E-P anchors (Fig. 2d,e and Supplementary Fig. 2a), we further investigated the functions of JMJD2 in regulation of E-P interactions, using mouse ES cells with conditional triple-knockout of *Jmjd2a*, *Jmjd2b* and *Jmjd2c*, given the redundant functions of these genes[22]. After depletion of JMJD2 by 4-hydroxytamoxifen (4-OHT) treatment for 72 h (denoted by 'TKO'), ES cells maintained their morphology with minimal changes in core pluripotent gene expression (Supplementary Fig. 2b,c), whereas JMJD2 became undetectable (Supplementary Fig. 2d,e). H3K27ac HiChIP[23] was performed to determine changes in E-P interactions (Supplementary Fig. 2f–h). *Jmjd2*-TKO ES cells showed a marked reduction in E-P interactions (Fig. 2f,g, Supplementary Fig. 2i and Supplementary Table 3). Although *Jmjd2*-TKO had a noticeable but limited effect on the LoopID target site *Oct4* E-P interaction (Fig. 2g), this may have been due to other remaining proteins within the looposome that help maintain this specific interaction. However, at a global level and in other more typical JMJD2-associated E-P interactions, the impact of *Jmjd2*-TKO on interaction strength was more pronounced (Fig. 2f and Supplementary Fig. 2i). Moreover, both H3K27ac HiChIP with a spike-in control[24] (Supplementary Fig. 2j–l) and Micro-C[25,26] (Supplementary Fig. 2m–o) demonstrated significant reductions in E-P interactions in response to JMJD2 depletion. Overall, these results indicate that JMJD2 proteins are critical mediators of E-P interactions.

In addition, LoopID performed on the *Oct4* E-P interaction showed that acute depletion of JMJD2 led to a significant reduction in components of the looposome (Fig. 2h–j), without obvious changes in expression of looposome factors (Supplementary Fig. 2p,q). Moreover, the regulatory function of JMJD2 was not restricted to *Oct4* E-P interaction but was also observed in other E-P interactions such as *Nanog* and *Sall1* (Supplementary Fig. 2r).

Taken together, these results demonstrate that JMJD2 plays a part in the maintenance of E-P interactions and the looposome (Fig. 2k).

JMJD2 forms biomolecular condensates

To investigate how JMJD2 regulates E-P interactions, we analyzed its structure and found that it contained large intrinsically disordered regions (IDRs) (Supplementary Fig. 3a), suggesting that its role in regulating E-P interactions may involve biomolecular condensate formation.

In vivo, IF with DNA fluorescence in situ hybridization (FISH) demonstrated that JMJD2 puncta were colocalized with E-P interaction sites (Fig. 3a and Supplementary Fig. 3b), and JMJD2 puncta were detectable using different antibodies across multiple cell lines (Supplementary Fig. 3c,d). Live-cell microscopy of endogenously tagged JMJD2 via fluorescent knock-in confirmed the presence of punctate structures (Supplementary Fig. 3e); fluorescence recovery after photobleaching experiments revealed the dynamic behavior of these puncta (Fig. 3b), and 1,6-hexanediol treatment reversibly disrupted them (Supplementary Fig. 3e). Moreover, overexpression experiments showed that compared to low overexpression levels, high overexpression levels resulted in significantly larger JMJD2 condensates (Supplementary Fig. 3f), consistent with the concentration-dependent nature of condensate formation[27]. These data suggest that JMJD2 is a biomolecular-condensate-forming protein in vivo. In vitro, the IDR of JMJD2 alone formed droplets in the presence of crowding agent PEG-8000, exhibiting concentration dependence, salt sensitivity and fluidity (Supplementary Fig. 3g,h). Full-length JMJD2 also formed fluid droplets (Supplementary Fig. 3i), whereas IDR truncation, which resulted in condensate-incapable mutants (denoted 'Mut'), severely impaired droplet formation and fluidity (Fig. 3d,e and Supplementary Fig. 3j–l), highlighting the critical role of the IDR in JMJD2 condensate formation. Notably, JMJD2 formed dynamic condensates under a physiological salt condition with H3K4me3-modified nucleosome arrays in the absence of PEG-8000, and IDR truncation similarly diminished this effect (Supplementary Fig. 3m). Mechanistically, the amino acid composition and dynamic state of the IDR provide a molecular basis for JMJD2's condensate formation (Supplementary Fig. 3n,o and Supplementary Note 2).

Taken together, these findings led us to conclude that JMJD2 forms biomolecular condensates both in vivo and in vitro, and that the IDR is indispensable for this process.

JMJD2 condensates contribute to maintaining E-P interactions

To evaluate the role of condensate formation in JMJD2's maintenance of E-P interactions, we expressed IDR-truncated JMJD2 mutants (Mut) in cells while depleting endogenous JMJD2 by 4-OHT treatment for 72 h. As expected, the Mut proteins showed impaired capacity to form condensates in vivo (Fig. 3d,e and Supplementary Fig. 3j). As JMJD2C is crucial for cell fate decision[28], we selected this protein for investigation of the roles of JMJD2 condensates in regulation of E-P interactions. H3K27ac HiChIP showed that ectopic expression of Mut inefficiently rescued the attenuated E-P interactions in TKO ES cells (72 h 4-OHT treatment, Fig. 3f–h and Supplementary Fig. 3p–r). To further validate the role of JMJD2 condensates in maintenance of E-P interactions, we generated two condensate-rescue mutants of JMJD2 by fusing two human IDRs (hIDR1 and hIDR2; Supplementary Table 4), to avoid the confounding effects of genetic background[29]. Compared to Mut, the condensate-rescue mutants of JMJD2 (denoted Mut-hIDR1 and Mut-hIDR2) were better able to form condensates both in vivo and in vitro (Fig. 3d,e and Supplementary Fig. 3j) and were more enriched at E-P anchors (Fig. 3i and Supplementary Fig. 3s). Notably, H3K27ac HiChIP showed that Mut-hIDRs efficiently rescued the attenuated E-P interactions in TKO ES cells (Fig. 3f–h). Furthermore, the superior ability of Mut-hIDR1 to rescue the attenuated E-P interactions compared with Mut is less likely to be attributable to an influence on the proteins interacting with JMJD2 (Supplementary Fig. 3t,u and Supplementary Table 5).

LoopID revealed that Mut-hIDR1 significantly rescued looposome proteins relative to *Jmjd2*-TKO, and rescued more proteins than Mut (Fig. 4a–d, Supplementary Fig. 4a,b and Supplementary Note 3). Consistently, enrichment of looposome components on E-P anchors (Fig. 4e and Supplementary Fig. 4c) and condensate formation of looposome components (Fig. 4f,g, Supplementary Fig. 4d–i and Supplementary Note 3) showed greater rescue effects with Mut-hIDRs compared to Mut.

Together, these results indicate that JMJD2 maintains E-P interactions and the looposome through formation of biomolecular condensates (Figs. 3j and 4h).

JMJD2 can maintain E-P in a catalytic-independent manner

Previous studies have shown that regulation of chromatin structure by ERs depends on their catalytic activity[30–33]. However, recent studies have revealed that the functions of many ERs extend beyond their catalytic activities in regulating transcription[34]. Therefore, we further explored

https://doi.org/10.1038/s41588-025-02415-8

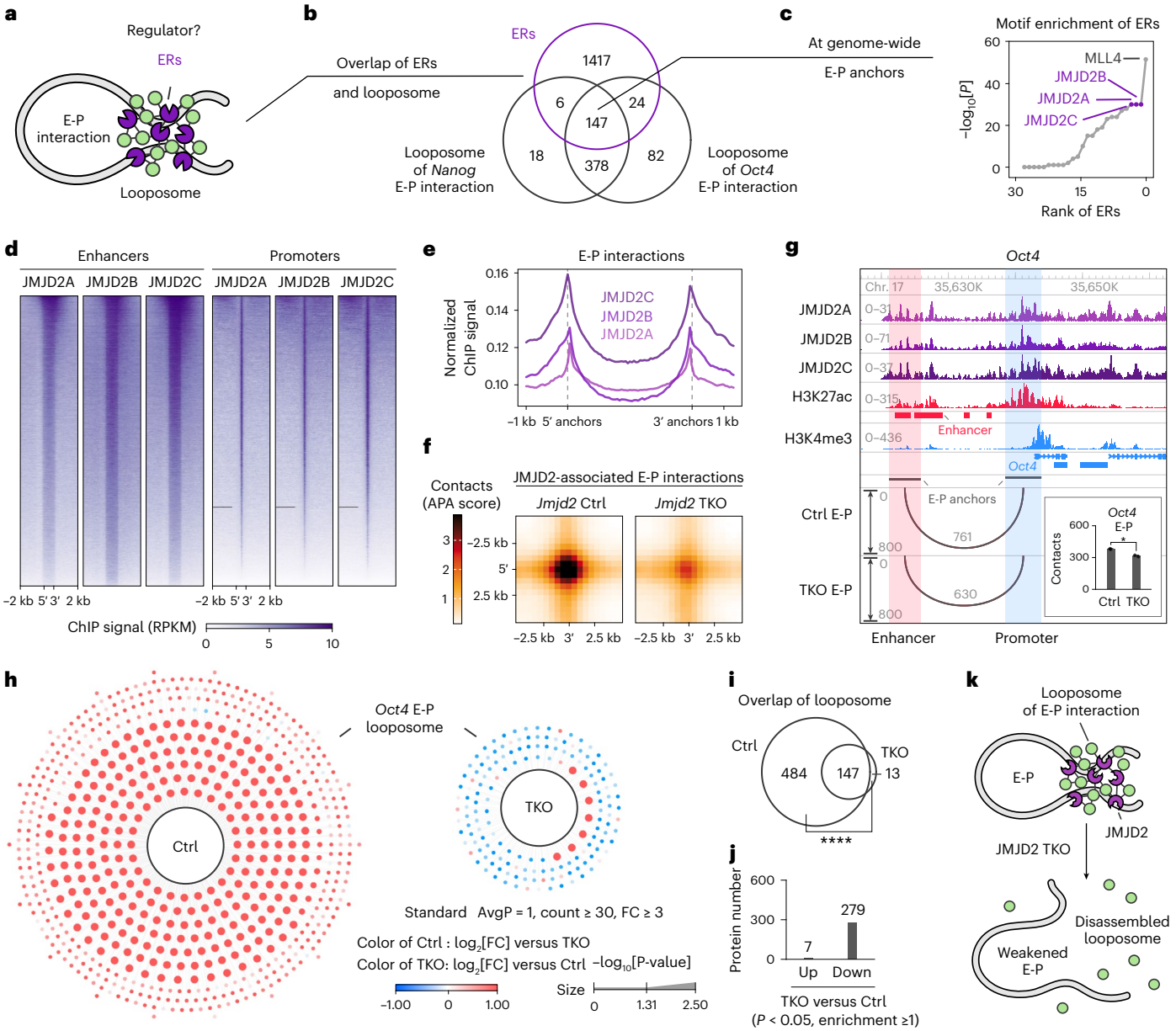

Fig. 2 | Histone demethylase JMJD2 maintains E-P interactions and looposome. **a**, Hypothetical diagram depicting ERs acting as regulators of E-P interactions. **b**, Venn diagram showing the overlap of known ERs and the indicated looposome. The overlapping proteins were identified as ER candidates for regulation of E-P interactions. **c**, Motif enrichment of ERs at genome-wide E-P anchors, based on public ChIP–seq data (see Methods for details). The *x* axis represents the rank of the candidate factors, and the *y* axis represents the $-\log_{10}[P]$ values of the motif enrichment. **d**, Heatmaps displaying the occupancy of JMJD2 proteins at genome-wide enhancers (identified by H3K27ac peaks) and promoters (transcription start site ±3 kb). **e**, Average plot showing enrichment of JMJD2 at genome-wide E-P interactions. **f**, Aggregate peak analysis (APA) of JMJD2-associated E-P interactions (details in Supplementary Table 3, $n = 7{,}414$) detected by H3K27ac HiChIP. The E-P strength is indicated by the extent of focal enrichment at the center of the plot. 'Ctrl' represents *Jmjd2*$^{fl/fl}$ ES cells, whereas 'TKO' represents *Jmjd2*$^{fl/fl}$ ES cells that were treated with 4-OHT for 72 h to deplete JMJD2A, JMJD2B and JMJD2C. **g**, Genome browser view showing the effect of JMJD2 depletion on *Oct4* E-P interaction. For ChIP–seq results, *y*-axis values represent RPKM for JMJD2 proteins[36] and histone modifications[50] from published studies in mES cells. For E-P interactions, *y*-axis values represent normalized combined contacts from the two replicates of Ctrl and TKO as annotated. The inset bar chart shows the mean ± s.e.m. of normalized contacts from two replicates of the indicated samples. The *P* value was determined by diffloop (see Methods for details, $n = 2$). **h**, Looposome of *Oct4* E-P interaction before and after JMJD2 depletion. The sizes of dots indicate the significance ($-\log_{10}[P]$), calculated by SAINTexpress (see Methods for details, $n = 2$). The color of Ctrl indicates the $\log_2$[FC] (Ctrl versus TKO), with red meaning that Ctrl is higher than TKO and blue that Ctrl is lower than TKO. The color of 'TKO' indicates the $\log_2$[FC] (TKO versus Ctrl), with red meaning that TKO is higher than Ctrl and blue that TKO is lower than Ctrl. **i**, Venn plot showing the overlap of the indicated looposome. The *P* value was determined using one-sided hypergeometric test. **j**, Bar chart showing numbers of significantly upregulated or downregulated proteins in the looposome after JMJD2 depletion; the *P* value was calculated by SAINTexpress with Bayesian FDR correction (see Methods for details, $n = 2$). **k**, Diagram depicting the role of JMJD2 in maintenance of E-P interactions and the looposome. *$P < 0.05$, **$P < 0.01$, ***$P < 0.001$, ****$P < 0.0001$.

the potential for JMJD2 condensates to maintain E-P interactions in a catalytic-independent manner.

We conducted a time dynamic analysis of JMJD2 depletion, identifying the earliest time point at which JMJD2 was observed to be completely depleted (36 h after 4-OHT treatment, denoted 'TKO 36 h') (Fig. 5a). The short-term depletion of JMJD2 barely affected JMJD2 substrate histone modifications (H3K9me3, H3K9me2 and H3K36me3) (Fig. 5b and Supplementary Fig. 5a,b), enhancer and promoter activities

(H3K27ac and H3K4me3) (Supplementary Fig. 5c), global gene expression (Supplementary Fig. 5c and Supplementary Table 6), cell cycle (Supplementary Fig. 5d,e), replication timing (Supplementary Fig. 5f–h), cell apoptosis (Supplementary Fig. 5i) and cell metabolism (Supplementary Fig. 5j), while significantly weakening E-P interactions (Fig. 5c and Supplementary Fig. 5k). In addition, acute depletion of looposome factors—CTCF, cohesin and YY1 (ref. 35), as well as SOX2 (Supplementary Fig. 5l)—can also destabilize E-P interactions without significantly altering gene expression, implying a broader functional relevance of looposome factors.

Further, H3K27ac HiChIP analysis revealed that transient ectopic expression of Mut-hIDR1 more effectively rescued the attenuated E-P interactions in TKO 36 h ES cells compared to Mut, without obvious alterations in H3K9me3 (Fig. 5b,c). In addition, unlike the dynamic scrambled IDR mutants (Mut-scrIDR1 and Mut-scrIDR2; Supplementary Note 2), which rescued the E-P interactions attenuated following JMJD2 depletion (36 h 4-OHT treatment), the solid-like Mut-DIX mutants (in which the IDR of JMJD2 was replaced by solid-like condensate core domain DIX; Supplementary Note 2) showed significantly impaired rescue capacity (Supplementary Fig. 5m). Moreover, the catalytic mutants (CMuts) of JMJD2[36], which formed biomolecular condensates (Supplementary Fig. 5n,o) but failed to demethylate H3K9me3 (Fig. 5b), also rescued the attenuated E-P interactions (Fig. 5c). These findings indicate that JMJD2 condensates can mediate E-P interactions without affecting their catalytic substrates. Consistently, LoopID assays revealed that TKO 36 h led to marked reductions in key looposome components on the *Oct4* E-P (Supplementary Fig. 5p). The disruption of the looposome in TKO 36 h ES cells was validated by proximity ligation assays combined with single-molecule DNA FISH on two known interacting protein pairs (YY1 and OCT4[37]; and BRD4 and NIPBL[38]) within the looposome. The results showed that numbers of interacting looposome proteins at the *Oct4* E-P site were significantly reduced (Supplementary Fig. 5q,r). Notably, ectopic expression of CMuts effectively rescued the disassembled looposome in TKO 36 h ES cell (Supplementary Fig. 5s). In summary, these results suggest that JMJD2 condensates maintain E-P interactions and looposome, most likely independently of catalytic activity.

JMJD2 CMuts alleviate JMJD2-TKO-induced ES cell state exit

Perturbation or induction of E-P interactions has been reported to influence the expression of associated genes and to be correlated with changes in cell fate[39,40]. In line with this, we found that the changes in pluripotent E-P interactions occurred earlier than the changes in gene expression and cell status following JMJD2 depletion (Supplementary Fig. 5t,u). Short-term depletion of JMJD2 (TKO 36 h) caused significant attenuation of pluripotent E-P interactions without immediate effects on the associated pluripotent gene expression, whereas long-term depletion (>2 weeks of 4-OHT treatment, denoted 'TKO long') downregulated many of these genes (Supplementary Fig. 5t,u) and coincided with ES cells exiting pluripotency and undergoing cell apoptosis (Fig. 5d and Supplementary Fig. 5v,w). Moreover, Mut-hIDR1 and CMuts more effectively alleviated the phenotypes caused by TKO long than Mut (Fig. 5d and Supplementary Fig. 5v,w). These results suggest that JMJD2 depletion or condensate mutations attenuate E-P interactions, possibly contributing to subsequent changes in ES cell state.

Taken together, these results indicate that JMJD2 condensates can maintain pluripotent E-P interactions in a catalytic-independent manner (Fig. 5e), disruption of which eventually attenuates ES cell self-renewal.

JMJD2 CMuts promote E-P of two-cell-specific genes

Next, we investigated the effects of overexpression of JMJD2 on E-P interactions and cellular states (Fig. 6a). Ectopic overexpression of condensate-competent JMJD2 activated multiple two-cell-specific genes, including *Zscan4*, in ES cells (Fig. 6b,c, Supplementary Fig. 6a,b and Supplementary Table 6) and promoted transition of ES cells to 2CLCs (Fig. 6d,e, Supplementary Fig. 6c–e and Supplementary Note 4).

Previous studies have shown that expression of two-cell-specific genes and developmental potency are closely related to E-P interactions[41,42]. Accordingly, we found that the frequency of *Zscan4* E-P interaction increased following JMJD2 overexpression and was correlated with condensate formation (Fig. 6f). These observations were consistent with binding of JMJD2 to two-cell-specific genes after overexpression, with greater enrichment of JMJD2 in cells expressing Mut-hIDR1 and CMuts than in those expressing Mut (Supplementary Fig. 6f) and activation of the associated genes (Supplementary Fig. 6g). Taken together, these results indicate that overexpression of condensate-competent JMJD2 can promote E-P interactions of two-cell-specific genes in ES cells.

Further, to investigate whether JMJD2 condensates could promote E-P interactions of two-cell-specific genes independently of catalytic activity, we transiently overexpressed various condensate mutants of JMJD2 in ES cells (Fig. 6g and Supplementary Fig. 6h). ChIP–seq and RNA sequencing (RNA-seq) results demonstrated that transient JMJD2 overexpression barely affected H3K9me3 levels (Fig. 6h) and gene expression (Supplementary Fig. 6h), whereas full-length, Mut-hIDR1 and CMuts of JMJD2 more strongly enhanced the E-P interactions of two-cell-specific genes including *Zscan4* compared to Mut (Fig. 6i and Supplementary Fig. 6i). Consistently, overexpression of scrambled IDR mutants (Mut-scrIDR1 and Mut-scrIDR2; Supplementary Fig. 6j)

Fig. 3 | JMJD2 maintains E-P interactions by forming biomolecular condensates. a, DNA FISH coupled with JMJD2 IF was used to show the colocalization of *Oct4* E-P anchors and JMJD2 condensates. **b**,**c**, Representative images and quantification ($n = 3$) of fluorescence recovery after photobleaching experiments with JMJD2 with knock-in of *mClover* in ES cells. The bleached area is highlighted by yellow boxes. **d**, Top: diagrams showing different mutations of JMJD2C protein, including full-length JMJD2C, IDR-truncated JMJD2C (Mut), IDR-truncated JMJD2C fused with hIDR1 or hIDR2 (Mut-hIDR1 or Mut-hIDR2), and hIDR1 or hIDR2 only. 'TKO' refers to results from the cell line that expressed an empty vector combined with 72 h 4-OHT treatment. Middle: representative IF images showing the condensates of the indicated proteins in vivo. Nuclear boundaries are indicated by white dotted lines. Bottom: droplet formation of the mEGFP-tagged proteins in vitro. The image in the 'TKO' column is from the droplet formation of mEGFP alone. **e**, Quantification of the puncta counts of the indicated proteins in vivo or in vitro. All *P* values were determined using two-sided Student's *t*-test ($n = 30$ fields of view; FOV). Data are presented as the mean ± s.e.m. **f**, APA analysis showing the effects of JMJD2 depletion (via 72 h 4-OHT treatment) or condensate disruption (via overexpression of the indicated mutants combined with 72 h 4-OHT treatment) on JMJD2-associated E-P interactions (H3K27ac HiChIP replicates $n = 2$). All *P* values were determined using two-sided Wilcoxon rank-sum test (JMJD2-associated E-P interactions $n = 7{,}414$). **g**, Genome browser view showing the effects of JMJD2 depletion or mutations on the *Oct4* E-P interaction. For ChIP–seq, the *y*-axis values represent RPKM for JMJD2 proteins[36] and histone modifications[50] from published studies in mES cells. For E-P interactions, the *y*-axis values represent the normalized combined contacts from two replicates of all the indicated samples (see Supplementary Table 3 for details), with numerical values annotated on the figure. **h**, Bar chart showing normalized contacts from two replicates of the indicated samples (see Supplementary Table 3 for details). Data are presented as the mean ± s.e.m. **i**, Flag ChIP–qPCR showing binding of the indicated proteins at *Oct4* E-P anchors. 'TKO' refers to results from the cell line that expressed an empty vector and were treated with 4-OHT for 72 h. All *P* values were determined using two-sided Student's *t*-test ($n = 3$ biologically independent experiments). Data are presented as mean ± s.e.m. **j**, Diagram showing that disruption of JMJD2 condensates attenuated E-P interactions, which could be rescued by the condensate-rescue mutants. $^{*}P < 0.05$, $^{**}P < 0.01$, $^{***}P < 0.001$, $^{****}P < 0.0001$.

https://doi.org/10.1038/s41588-025-02415-8

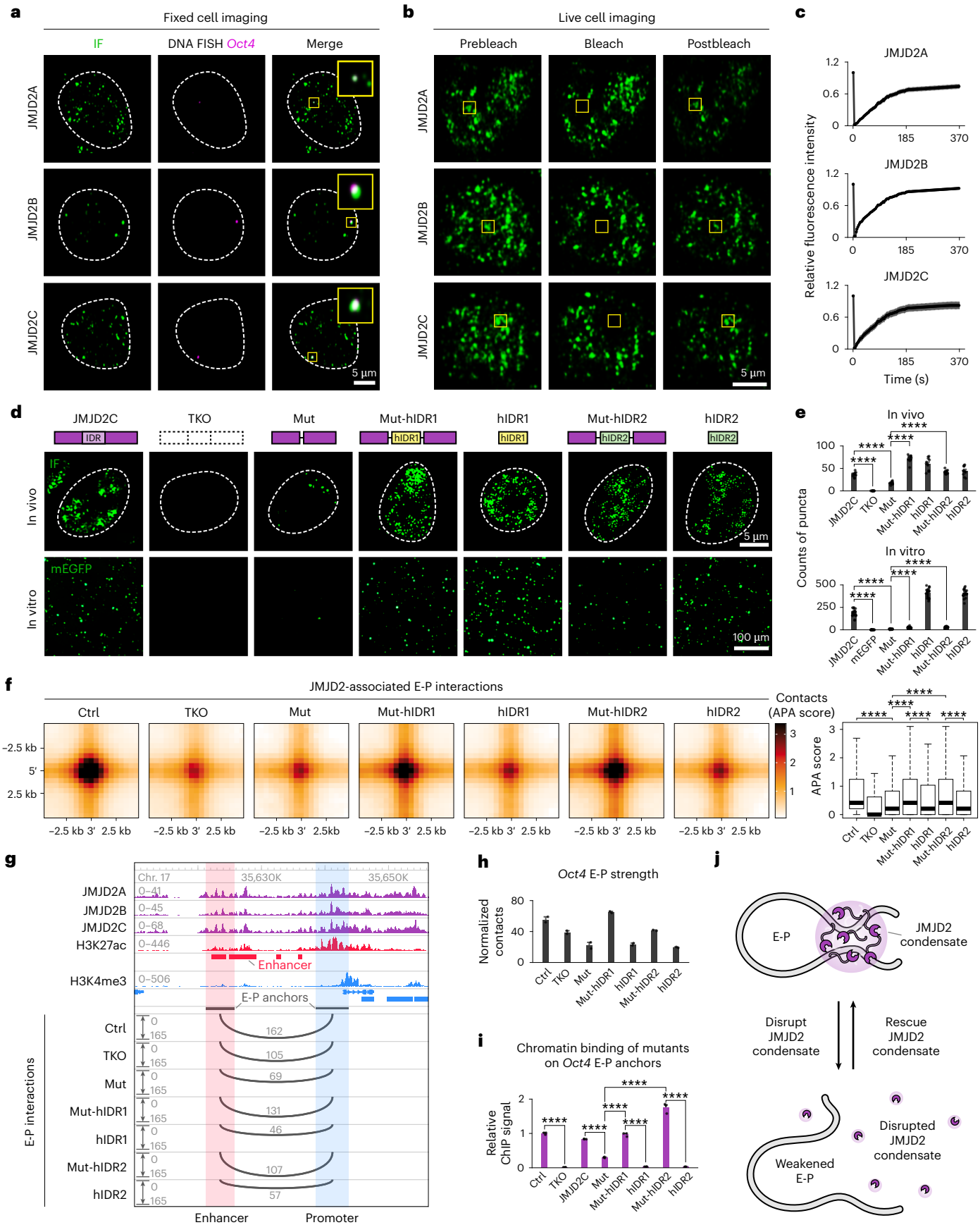

https://doi.org/10.1038/s41588-025-02415-8

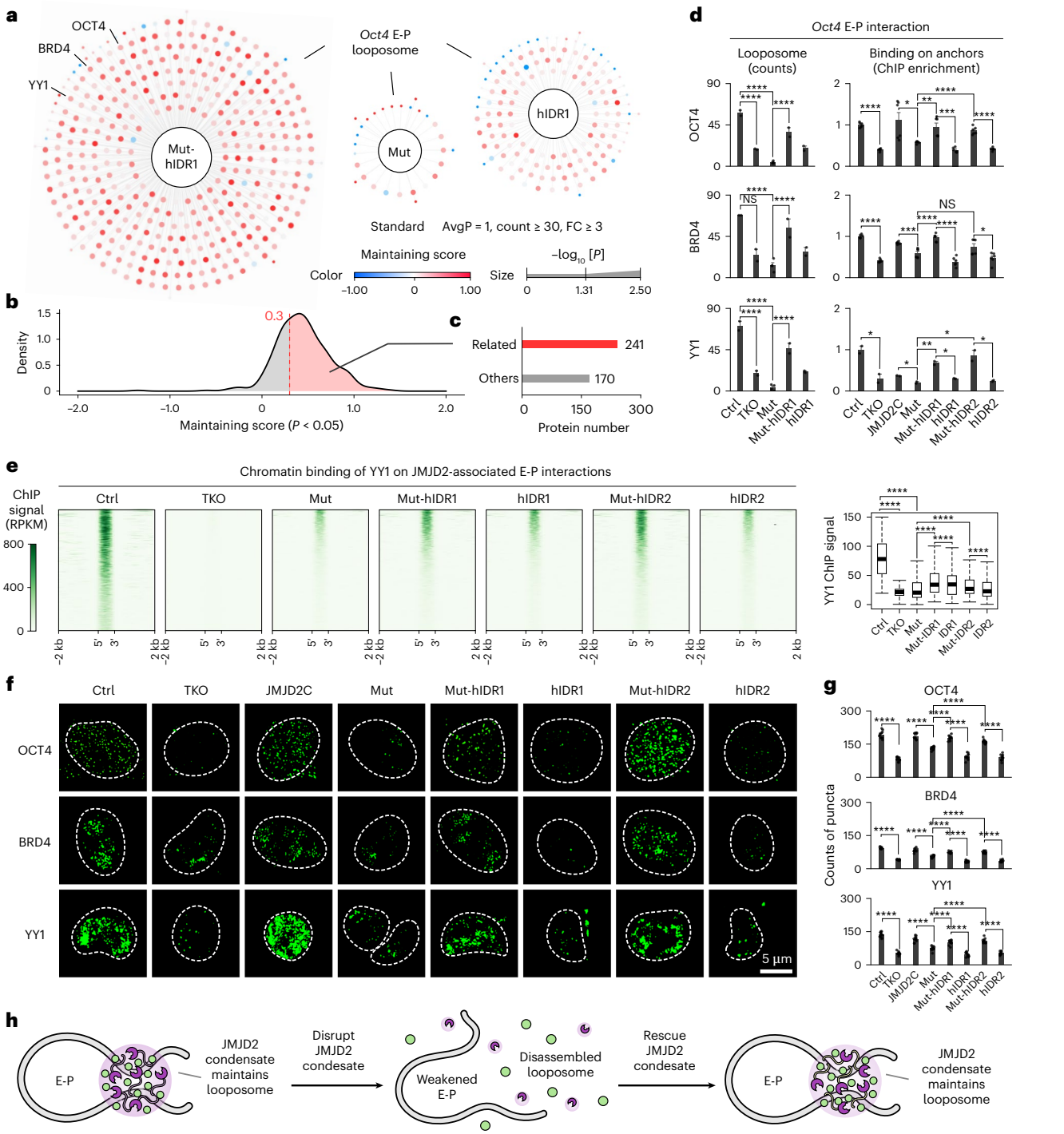

Fig. 4 | JMJD2 maintains the looposome by forming biomolecular condensates. **a**, Looposomes of *Oct4* E-P interaction in TKO ES cells (72 h 4-OHT treatment) with expression of the indicated mutants. A maintaining score was used to indicate the correlation between the enrichment of the protein in looposome and the condensate-forming ability of JMJD2. A higher score indicates increased likelihood of protein maintenance in the looposome rescued by JMJD2 condensates. The size of the circle represents the significance (details in Methods, $n = 2$). **b**, Density plot showing the distribution of the maintaining score. Proteins with maintaining scores higher than 0.3 were identified as JMJD2 condensate-related looposome proteins. **c**, Bar chart showing numbers of looposome proteins related or unrelated to JMJD2 condensates. **d**, Bar charts displaying the peptide counts or relative binding of the indicated looposome proteins on *Oct4* E-P anchors compared to Ctrl. Protein binding was detected by ChIP–qPCR. For the looposome, *P* values were determined by SAINTexpress (details in Methods, $n = 2$). For ChIP–qPCR, *P* values were determined by two-sided Student's *t*-test ($n = 3$ biologically independent experiments). Data are presented as the mean ± s.e.m. **e**, Heatmap and box plot showing effects of JMJD2 depletion (via 72 h 4-OHT treatment) or condensate disruption (via overexpression of the indicated mutants combined with 72 h 4-OHT treatment) on chromatin binding of YY1 at JMJD2-associated E-P anchors. All *P* values were determined using two-sided Wilcoxon rank-sum test (YY1 ChIP–seq replicates $n = 2$, YY1 peaks on JMJD2-associated E-P interactions $n = 6{,}519$). **f**, Representative IF images displaying the condensates of the indicated looposome factors. Both the TKO and mutant-overexpressing cell lines were treated with 4-OHT for 72 h. **g**, Quantification of the counts of condensates. All *P* values were determined by two-sided Student's *t*-test ($n = 30$ FOVs). Data are presented as the mean ± s.e.m. **h**, Diagram showing that disruption of JMJD2 condensates attenuated the looposome, an effect that was rescued by condensate-rescue mutants of JMJD2. $^{*}P < 0.05$, $^{**}P < 0.01$, $^{***}P < 0.001$, $^{****}P < 0.0001$. NS, not significant.

https://doi.org/10.1038/s41588-025-02415-8

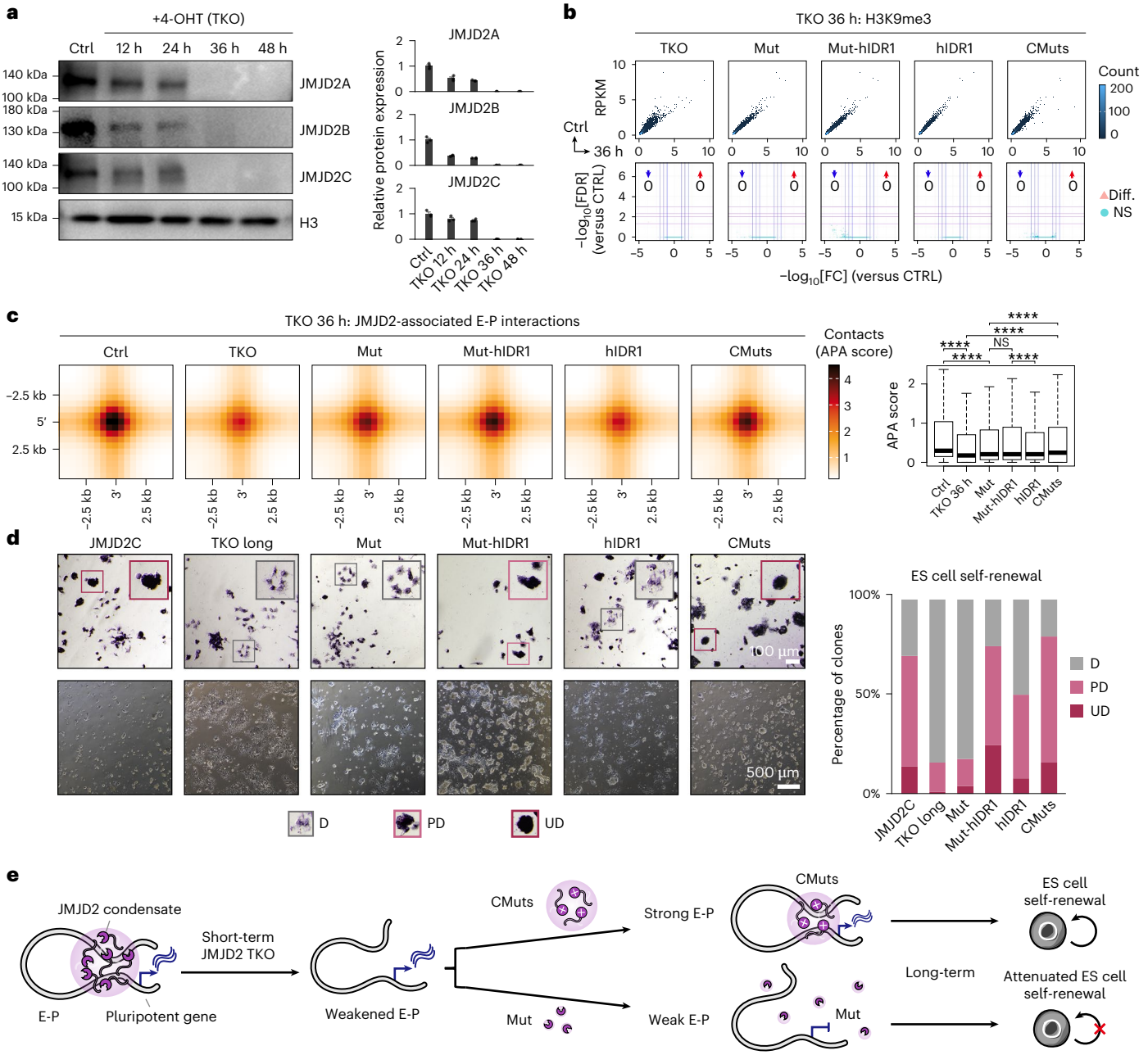

Fig. 5 | JMJD2 condensates can maintain pluripotent E-P interactions in ES cells in a catalytic-independent manner. a, Western blotting results showing temporal dynamic quantification of chromatin-bound JMJD2 in Ctrl cells treated with 4-OHT. H3 was used as a loading control. Data are plotted as the mean ± s.e.m. **b**, Top: scatter plots showing overall signal changes in H3K9me3 ChIP–seq. Bottom: volcano plots showing results of differential analysis. Numbers of significant upregulated and downregulated bins are annotated in the plot (FDR < 0.05 and absolute value of $\log_2$[FC] > 1). The differential analysis was performed using DiffBind (see Methods for details, $n = 2$). **c**, APA analysis showing effects of JMJD2 depletion or condensate disruption on JMJD2-associated E-P interactions (H3K27ac HiChIP replicates $n = 2$). 'TKO 36 h' indicates that both the TKO (cells expressing an empty vector) and mutant-overexpressing cell lines were treated with 4-OHT for 36 h. All *P* values were determined using two-sided Wilcoxon rank-sum test (JMJD2-associated E-P interactions $n = 7{,}414$). **d**, Alkaline phosphatase staining (top) and morphology (bottom) showing that Mut-hIDR1 and CMuts rescued the morphology of ES cells that had been altered by prolonged JMJD2 depletion (more than 1 week of 4-OHT treatment) more efficiently than hIDR1 and Mut. Colonies were stained for alkaline phosphatase activity and grouped into three categories: differentiated (D), partially differentiated (PD) and undifferentiated (UD). Percentages for each category are quantified ($n = 4$ FOVs). **e**, Diagram showing that JMJD2 condensates can maintain E-P interactions in a catalytic-independent manner. $^*P < 0.05$, $^{**}P < 0.01$, $^{***}P < 0.001$, $^{****}P < 0.0001$. Diff., significantly different.

also promoted ES cell-to-2CLC transitions (Supplementary Fig. 6k,l) and activated two-cell-specific genes (Supplementary Fig. 6m), whereas solid-like condensate mutant Mut-DIX severely impaired this process (Supplementary Fig. 6j–m). Moreover, transient overexpression (36 h) of Mut-scrIDRs more effectively enhanced E-P interactions of key two-cell-specific genes *Zscan4*c and *Nelfa* than Mut-DIX (Supplementary Fig. 6n). These results demonstrate that JMJD2 condensates can promote E-P interactions of two-cell-specific genes, most likely independently of catalytic activity (Fig. 6j), whereas the selective mediation of pluripotent and two-cell-specific E-P interactions by JMJD2 before and after overexpression might be due to its dosage in ES cells (Supplementary Fig. 6o–z and Supplementary Note 5).

https://doi.org/10.1038/s41588-025-02415-8

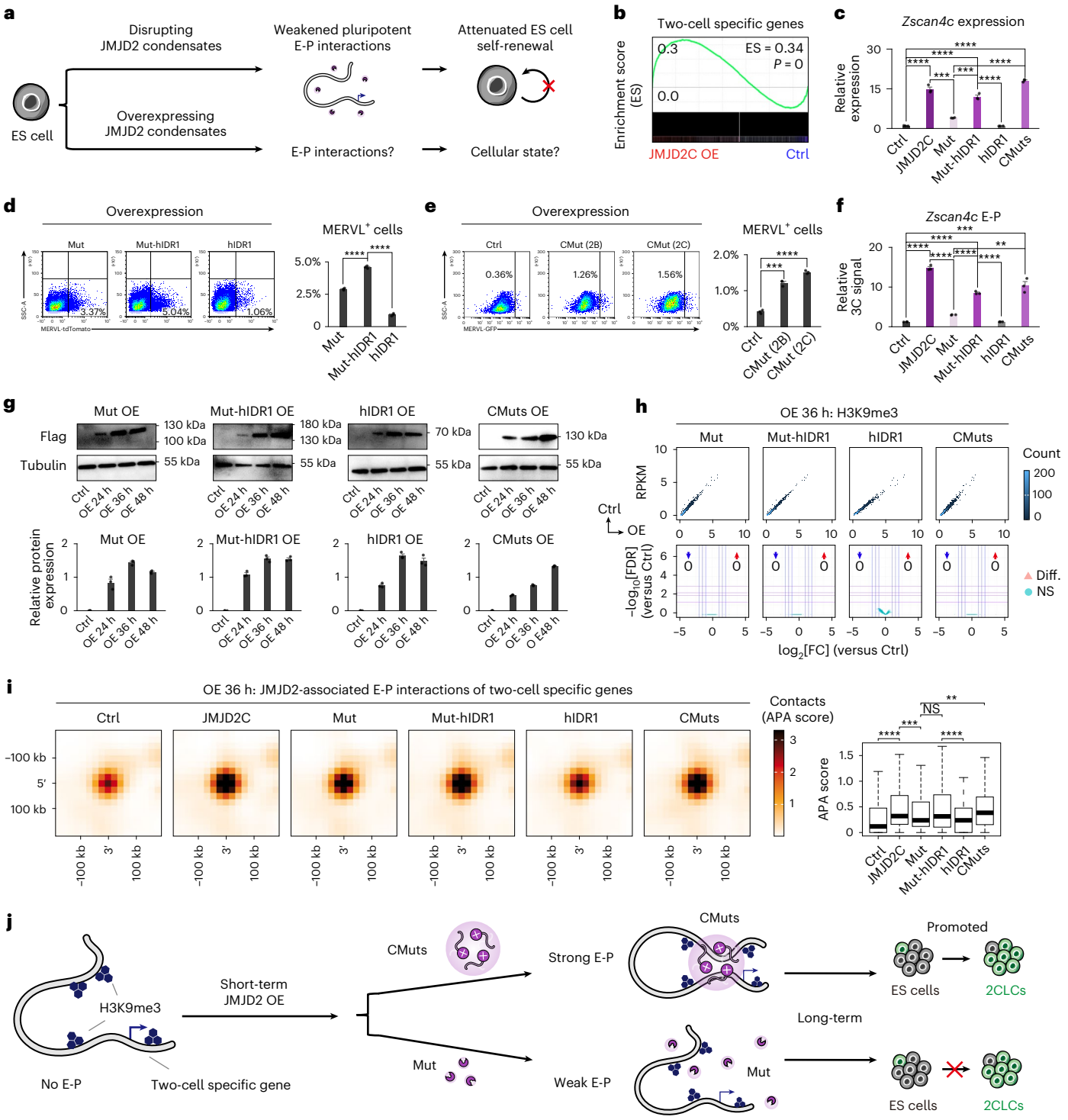

Engineering E-P interactions of two-cell-specific genes through JMJD2 condensates

As JMJD2 condensates could regulate E-P interactions and cellular states, we explored whether assembling JMJD2 condensates at specific genomic loci could enable us to engineer cell-type-specific E-P interactions and promote cell fate transition. To this end, we designed a dCas9-based chemically inducible system to guide JMJD2 condensates to specific E-P anchors for E-P engineering[40] (Fig. 7a). SadCas9-ABI and SpdCas9-PYL, both fused with JMJD2 protein mutants, were introduced by site-specific sgRNAs to the targeted enhancer and promoter, respectively, to induce E-P interaction de novo with addition of inducer abscisic acid (ABA) (Fig. 7a). Whereas the published E-P engineering system requires continuous induction[40,43] (Supplementary Fig. 7a), we anticipated that our condensate-containing system would not only establish the targeted E-P interactions upon induction but also retain the interactions after removal of the chemical, which could eventually facilitate cell fate transition (Fig. 7a).

The E-P engineering system was applied to establish E-P interactions for two key two-cell-specific genes, *Zscan4* and *Nelfa*, in ES cells (Fig. 7b,c). The two target genes were selected because they are highly expressed in 2CLCs but silenced in ES cells[44], and their overexpression enhances the developmental potency of ES cells[44,45].

https://doi.org/10.1038/s41588-025-02415-8

Fig. 6 | JMJD2 condensates can promote two-cell specific E-P interactions after overexpression in a catalytic-independent manner. a, Diagram showing that disrupting JMJD2 condensates attenuated pluripotent E-P interactions and ES cell self-renewal, whereas further exploration is needed to understand the impact of overexpression of JMJD2 condensates on E-P interactions and cellular state. **b**, Gene set enrichment analysis plot showing that ES cells overexpressing full-length JMJD2 showed greater enrichment in expression of two-cell specific genes compared to Ctrl. The *P* value was determined by gene set enrichment analysis (one-sided, see Methods for details; gene lists are detailed in Supplementary Table 7; $n = 7{,}892$). **c**, Relative expression of *Zscan4c* after overexpression of different JMJD2 mutants compared to Ctrl, as detected by quantitative PCR with reverse transcription. All *P* values were determined by two-sided Student's *t*-test ($n = 3$ biologically independent experiments). Data are presented as the mean ± s.e.m. **d**,**e**, For overexpression of JMJD2 condensate-related mutants (**d**) and catalytic mutants (**e**); left: FACS analysis showing the MERVL$^+$ population following ectopic overexpression of different mutants of JMJD2. Right: column graph summarizing the percentage of MERVL$^+$ cells. All *P* values were determined using two-sided Student's *t*-test ($n = 3$ biologically independent experiments). Data are presented as the mean ± s.e.m. **f**, Relative E-P strength of *Zscan4c* after overexpression of different JMJD2 mutants compared to Ctrl, as detected by 3C–qPCR. All *P* values were determined by two-sided Student's *t*-test ($n = 3$ biologically independent experiments). Data are presented as the mean ± s.e.m. **g**, Temporal dynamic quantification of JMJD2 mutants after transient overexpression using western blot analysis, with Tubulin serving as the loading control ($n = 3$ biologically independent experiments). OE, overexpression. Data are plotted as the mean ± s.e.m. **h**, Top: scatter plots showing overall ChIP–seq signal changes. 'OE 36 h' denotes cell lines in which the indicated mutants were transiently overexpressed for 36 h. Bottom: volcano plots showing results of differential analysis. Numbers of significant upregulated and downregulated bins are annotated in the plot (FDR < 0.05 and absolute value of $\log_2$[FC] > 1). The differential analysis was performed using DiffBind (see Methods for details; $n = 2$). **i**, APA analysis showing the effects of transient JMJD2 overexpression on JMJD2-associated E-P interactions of two-cell-specific genes (identified by Micro-C, overlapped with JMJD2 peaks after overexpression). 'OE 36 h' denotes cell lines in which the indicated mutants were transiently overexpressed for 36 h. All *P* values were determined using two-sided Wilcoxon rank-sum test (Micro-C replicates $n = 2$, JMJD2-associated E-P interactions of two-cell specific genes $n = 946$; details in Supplementary Table 3). **j**, Diagram showing that JMJD2 can promote two-cell specific E-P interactions after overexpression in a catalytic-independent manner. *$P < 0.05$, **$P < 0.01$, ***$P < 0.001$, ****$P < 0.0001$.

Regarding the targeted enhancers, the activation of *Zscan4* in two-cell embryos requires interaction with the targeted SE located 2 Mb downstream[42], whereas silencing of *Nelfa* in ES cells is related to a topologically associating domain boundary separating its promoter from the targeted enhancer[46]. Therefore, we hypothesized that engineering these E-P interactions through JMJD2 condensates could activate *Zscan4* and *Nelfa*, inducing a two-cell-like state in ES cells. In ES cells labeled with a ZSCAN4-GFP::MERVL-tdTomato double reporter to indicate ES cell-to-2CLC transition[47], *SadCas9-ABI* and *SpdCas9-PYL*, both fused with *Mut-hIDR1*, *Mut*, *hIDR1* or *CMuts* were introduced by site-specific sgRNAs to the targeted enhancer and promoter (Fig. 7c and Supplementary Fig. 7b). As expected, the targeted E-P interactions were facilitated by 96 h of ABA treatment and maintained constantly after ABA was withdrawn for 72 h (labeled '168 h') by Mut-hIDR1 (Fig. 7d and Supplementary Fig. 7c–e), which formed condensates at the targeted E-P anchors (Supplementary Fig. 7f). Similar to Mut-hIDR1, CMuts that were capable of forming condensates also constantly maintained E-P interactions after ABA was withdrawn (Fig. 7d and Supplementary Fig. 7g). Notably, Mut-hIDR1 and CMuts exhibited significantly higher efficiency in maintaining these interactions compared to Mut (Fig. 7d). These results indicate that assembling condensate-competent JMJD2 at specific genomic loci in ES cells is more efficient at engineering the E-P interactions of two-cell-specific genes than using condensate-incapable mutants.

Next, we investigated whether the transition of ES cells to 2CLCs was promoted following assembly of JMJD2 condensates at specific genomic loci. Compared to hIDR1 and Mut, the assembled Mut-hIDR1 and CMuts at specific E-P anchors more efficiently increased the population of 2CLCs in ES cells and activated two-cell-specific genes (Fig. 7e and Supplementary Fig. 7h,i). These results indicate that assembly of condensate-competent JMJD2 (Mut-hIDR1 or CMuts) at the targeted E-P anchors more effectively promotes ES cell-to-2CLC transition than use of condensate-incapable mutants (Mut) (Fig. 7f). Furthermore, the E-P engineering system was used to engineer pluripotent E-P interactions and induce pluripotency reprogramming (Supplementary Fig. 7j–t and Supplementary Note 6).

Taking these findings together, we conclude that assembling JMJD2 condensates at certain genomic loci enables engineering of cell-type-specific E-P interactions and promotes cell fate transition (Fig. 7f).

Discussion

In this study, we developed a chromatin-interaction-based proteomic approach called LoopID and found that the histone demethylase JMJD2 could mediate E-P interactions in a catalytic-independent manner through formation of biomolecular condensates. Cell-type-specific E-P interactions can be engineered by leveraging this mechanism to facilitate the recruitment of looposome factors to designated E-P site (Supplementary Fig. 7u–x and Supplementary Note 7), ultimately promoting cell fate transitions.

Chromatin interactions, which provide the structural basis of gene expression and cellular functions[48], are predominantly mediated by structural regulators. LoopID, which is based on chromatin interactions and has a higher signal-to-noise ratio compared to published locus-specific proteomic methods (summarized in Supplementary Table 2), can be useful in identifying potential chromatin structural regulators, particularly in specific cell types or biological processes. For example, we found that the ER JMJD2 could regulate E-P interactions in ES cells and 2CLCs. In addition, LoopID can be used to understand the varying impact of a factor on different E-P interactions. For instance, the effect of *Jmjd2*-TKO on different JMJD2-associated E-P interactions varied, possibly owing to contributions from other factors within the looposome to the structure. Moreover, several studies have demonstrated that abnormal chromatin organization is a major factor in anomalous embryonic development and disease[49], although the underlying mechanisms have

Fig. 7 | Engineering two-cell-specific E-P interactions and enhancing ES cell-to-2CLC transition via JMJD2 condensate assembly at certain genomic loci. **a**, Schematic depiction of the strategy and expected outcomes of engineering E-P interactions by assembling JMJD2 condensates at specific genomic loci. **b**, Timeline showing the treatments for engineering of E-P interactions. **c**, Genome browser view showing the targeted E-P interactions. The enhancers and promoters are indicated by H3K27ac and H3K4me3 ChIP–seq in 2CLCs, respectively[46], and the E-P interactions are identified by Hi-C in 2CLCs[46]. **d**, Relative strengths of E-P interactions and relative gene expression compared to 0 h. 'Mut', 'Mut-hIDR1', 'hIDR1' and 'CMuts' refer to the corresponding cell lines after E-P engineering. All *P* values were determined by two-sided Student's *t*-test ($n = 3$ biologically independent experiments). Data are presented as the mean ± s.e.m. **e**, Left: FACS analysis showing the 2CLC population. Right: bar chart summarizing the percentages of ZSCAN4C-GFP and MERVL-tdTomato double-positive cells. All *P* values were determined using two-sided Student's *t*-test ($n = 3$ biologically independent experiments). Data are presented as the mean ± s.e.m. **f**, Diagram showing that assembling JMJD2 condensates at certain genomic loci can engineer cell-type specific E-P interactions and promote cell fate transition. iPS cell, induced pluripotent stem cell; pre-iPS cell, preinduced pluripotent stem cell. *$P < 0.05$, **$P < 0.01$, ***$P < 0.001$, ****$P < 0.0001$.

https://doi.org/10.1038/s41588-025-02415-8

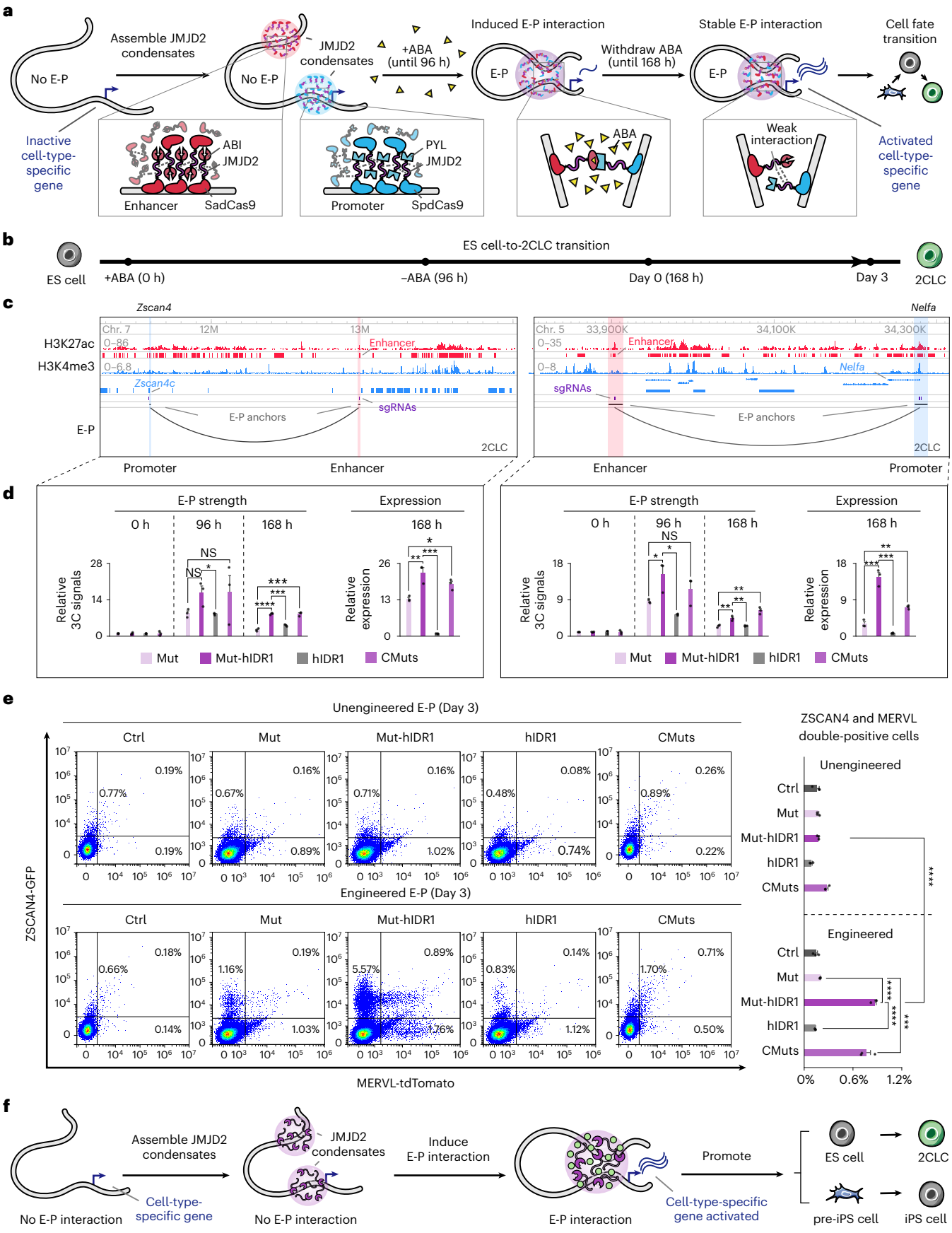

remained unclear. Notably, pathogenic chromatin interactions can occur independently of known architectural factors[10]. LoopID can be applied to explore the chromatin-structure-based proteomes involved in disease-associated chromatin reorganization and thereby identify potential therapeutic targets. Nevertheless, LoopID has limitations (Supplementary Note 8), and we recommend several strategies to enhance its specificity and reliability: (1) using non-sgRNA controls to account for background from random enzyme reconstitution; (2) designing at least three sgRNAs at each end and prioritizing those whose potential off-target sites lacked chromatin interactions (Supplementary Fig. 7y), as LoopID relies on such interactions for protein labeling—off-target dCas9 binding alone cannot reconstitute the active enzyme or trigger protein biotinylation; and (3) validating results through switched LoopID designs or replication in diverse cell lines if available. In addition, targeting non-interacting genomic regions may serve as an optional strategy to further reduce background.

The ER JMJD2 can regulate chromatin structure independently of its catalytic activity by forming condensates. This mechanism, which is applicable across various contexts, suggests a universal mode of action for JMJD2 and potentially other ERs; they may facilitate pre-establishment of E-P interactions of other lineages without altering repressive chromatin modifications and thus preparation for cell fate transition. Recent studies have also revealed that some ERs can sometimes regulate transcription independently of their catalytic activity through interactions with other transcriptional regulatory factors[34]. In this case, our findings suggest an alternative perspective in which epigenetic modifiers may achieve catalytic-independent transcription regulation by modulating chromatin structure.

Online content

Any methods, additional references, Nature Portfolio reporting summaries, source data, extended data, supplementary information, acknowledgements, peer review information; details of author contributions and competing interests; and statements of data and code availability are available at https://doi.org/10.1038/s41588-025-02415-8.

References

1. Heinz, S. et al. The selection and function of cell type-specific enhancers. *Nat. Rev. Mol. Cell Biol.* **16**, 144–154 (2015).
2. Hnisz, D. et al. Super-enhancers in the control of cell identity and disease. *Cell* **155**, 934–947 (2013).
3. Bonev, B. et al. Organization and function of the 3D genome. *Nat. Rev. Genet.* **17**, 772 (2016).
4. Krijger, P. H. L. et al. Regulation of disease-associated gene expression in the 3D genome. *Nat. Rev. Mol. Cell Biol.* **17**, 771–782 (2016).
5. Hnisz, D. et al. A phase separation model for transcriptional control. *Cell* **169**, 13–23 (2017).
6. Boija, A. et al. Transcription factors activate genes through the phase-separation capacity of their activation domains. *Cell* **175**, 1842–1855 (2018).
7. Sabari, B. R. et al. Coactivator condensation at super-enhancers links phase separation and gene control. *Science* **361**, aar3958 (2018).
8. Wang, W. et al. A histidine cluster determines YY1-compartmentalized coactivators and chromatin elements in phase-separated enhancer clusters. *Nucleic Acids Res.* **50**, 4917–4937 (2022).
9. Weintraub, A. S. et al. YY1 is a structural regulator of enhancer-promoter loops. *Cell* **171**, 1573–1588 (2017).
10. Ahn, J. H. et al. Phase separation drives aberrant chromatin looping and cancer development. *Nature* **595**, 591–595 (2021).
11. Cho, K. F. et al. Split-TurboID enables contact-dependent proximity labeling in cells. *Proc. Natl Acad. Sci. USA* **117**, 12143–12154 (2020).
12. Costa, Y. et al. NANOG-dependent function of TET1 and TET2 in establishment of pluripotency. *Nature* **495**, 370–374 (2013).
13. Ding, J. et al. Oct4 links multiple epigenetic pathways to the pluripotency network. *Cell Res.* **22**, 155–167 (2012).
14. Mumbach, M. R. et al. Enhancer connectome in primary human cells identifies target genes of disease-associated DNA elements. *Nat. Genet.* **49**, 1602–1612 (2017).
15. Peng, T. et al. STARR-seq identifies active, chromatin-masked, and dormant enhancers in pluripotent mouse embryonic stem cells. *Genome Biol.* **21**, 243 (2020).
16. Chen, H. et al. Dynamic interplay between enhancer-promoter topology and gene activity. *Nat. Genet.* **50**, 1296–1303 (2018).
17. Teo, G. et al. SAINTexpress: improvements and additional features in Significance Analysis of INTeractome software. *J. Proteomics* **100**, 37–43 (2014).
18. Branon, T. C. et al. Efficient proximity labeling in living cells and organisms with TurboID. *Nat. Biotechnol.* **36**, 880–887 (2018).
19. Ji, X. et al. Chromatin proteomic profiling reveals novel proteins associated with histone-marked genomic regions. *Proc. Natl Acad. Sci. USA* **112**, 3841–3846 (2015).
20. Hammal, F. et al. ReMap 2022: a database of human, mouse, Drosophila and Arabidopsis regulatory regions from an integrative analysis of DNA-binding sequencing experiments. *Nucleic Acids Res.* **50**, D316–D325 (2022).
21. Tsukada, Y. et al. Histone demethylation by a family of JmjC domain-containing proteins. *Nature* **439**, 811–816 (2006).
22. Pedersen, M. T. et al. Continual removal of H3K9 promoter methylation by Jmjd2 demethylases is vital for ESC self-renewal and early development. *EMBO J.* **35**, 1550–1564 (2016).
23. Mumbach, M. R. et al. HiChIP: efficient and sensitive analysis of protein-directed genome architecture. *Nat. Methods* **13**, 919–922 (2016).
24. Gryder, B. E. et al. Measurement of differential chromatin interactions with absolute quantification of architecture (AQuA-HiChIP). *Nat. Protoc.* **15**, 1209–1236 (2020).
25. Krietenstein, N. et al. Ultrastructural details of mammalian chromosome architecture. *Mol. Cell* **78**, 554–565 (2020).
26. Hsieh, T. S. et al. Resolving the 3D landscape of transcription-linked mammalian chromatin folding. *Mol. Cell* **78**, 539–553 (2020).
27. Alberti, S. et al. Considerations and challenges in studying liquid-liquid phase separation and biomolecular condensates. *Cell* **176**, 419–434 (2019).
28. Tomaz, R. A. et al. Jmjd2c facilitates the assembly of essential enhancer-protein complexes at the onset of embryonic stem cell differentiation. *Development* **144**, 567–579 (2017).
29. Bracha, D. et al. Mapping local and global liquid phase behavior in living cells using photo-oligomerizable seeds. *Cell* **175**, 1467–1480 (2018).
30. Jiang, Y. et al. The methyltransferase SETDB1 regulates a large neuron-specific topological chromatin domain. *Nat. Genet.* **49**, 1239–1250 (2017).
31. Yan, J. et al. Histone H3 lysine 4 monomethylation modulates long-range chromatin interactions at enhancers. *Cell Res.* **28**, 204–220 (2018).
32. Yan, Z. et al. G9a/GLP-sensitivity of H3K9me2 demarcates two types of genomic compartments. *Genomics Proteomics Bioinformatics* **18**, 359–370 (2020).
33. Montavon, T. et al. Complete loss of H3K9 methylation dissolves mouse heterochromatin organization. *Nat. Commun.* **12**, 4359 (2021).
34. Morgan, M. A. J. et al. Epigenetic moonlighting: catalytic-independent functions of histone modifiers in regulating transcription. *Sci. Adv.* **9**, eadg6593 (2023).

35. Hsieh, T. S. et al. Enhancer-promoter interactions and transcription are largely maintained upon acute loss of CTCF, cohesin, WAPL or YY1. *Nat. Genet.* **54**, 1919–1932 (2022).
36. Das, P. P. et al. Distinct and combinatorial functions of Jmjd2b/Kdm4b and Jmjd2c/Kdm4c in mouse embryonic stem cell identity. *Mol. Cell* **53**, 32–48 (2014).
37. Wang, J. et al. YY1 positively regulates transcription by targeting promoters and super-enhancers through the BAF complex in embryonic stem sells. *Stem Cell Rep.* **10**, 1324–1339 (2018).
38. Olley, G. et al. BRD4 interacts with NIPBL and BRD4 is mutated in a Cornelia de Lange-like syndrome. *Nat. Genet.* **50**, 329–332 (2018).
39. Schoenfelder, S. et al. Long-range enhancer-promoter contacts in gene expression control. *Nat. Rev. Genet.* **20**, 437–455 (2019).
40. Morgan, S. L. et al. Manipulation of nuclear architecture through CRISPR-mediated chromosomal looping. *Nat. Commun.* **8**, 15993 (2017).
41. Le, R. et al. Dcaf11 activates Zscan4-mediated alternative telomere lengthening in early embryos and embryonic stem cells. *Cell Stem Cell* **28**, 732–747 (2021).
42. Chen, M. et al. Chromatin architecture reorganization in murine somatic cell nuclear transfer embryos. *Nat. Commun.* **11**, 1813 (2020).
43. Wang, J. et al. Phase separation of OCT4 controls TAD reorganization to promote cell fate transitions. *Cell Stem Cell* **28**, 1868–1883 (2021).
44. Hu, Z. et al. Maternal factor NELFA drives a 2C-like state in mouse embryonic stem cells. *Nat. Cell Biol.* **22**, 175–186 (2020).
45. Amano, T. et al. Zscan4 restores the developmental potency of embryonic stem cells. *Nat. Commun.* **4**, 1966 (2013).
46. Zhu, Y. et al. Relaxed 3D genome conformation facilitates the pluripotent to totipotent-like state transition in embryonic stem cells. *Nucleic Acids Res.* **49**, 12167–12177 (2021).
47. Yang, F. et al. DUX-miR-344-ZMYM2-mediated activation of MERVL LTRs induces a totipotent 2C-like state. *Cell Stem Cell* **26**, 234–250 (2020).
48. Kadauke, S. et al. Chromatin loops in gene regulation. *Biochim. Biophys. Acta* **1789**, 17–25 (2009).
49. Anania, C. et al. Order and disorder: abnormal 3D chromatin organization in human disease. *Brief. Funct. Genomics* **19**, 128–138 (2020).
50. Shen, Y. et al. A map of the *cis*-regulatory sequences in the mouse genome. *Nature* **488**, 116–120 (2012).
51. Wang, J. et al. A comprehensive atlas of epigenetic regulators reveals tissue-specific epigenetic regulation patterns. *Epigenetics* **18**, 2139067 (2023).
52. Hu, H. et al. AnimalTFDB 3.0: a comprehensive resource for annotation and prediction of animal transcription factors. *Nucleic Acids Res.* **47**, D33–D38 (2019).

[1]Department of Rehabilitation Medicine, The Seventh Affiliated Hospital, Zhongshan School of Medicine, Sun Yat-Sen University, Guangdong, China. [2]Cancer Institute, Cellular Therapeutics School of Medicine, Xuzhou Medical University, Jiangsu, China; School of Basic Medical Sciences, Guangdong Medical University, Guangdong, China. [3]Frontiers Medical Center, Tianfu Jincheng Laboratory; Department of Gynecology and Obstetrics, West China Second Hospital; West China Biomedical Big Data Center, West China Hospital/West China School of Medicine, Sichuan University, Chengdu, China. [4]Shenzhen Eye Hospital, Shenzhen Eye Medical Center, Southern Medical University, Shenzhen, China. [5]State Key Laboratory of Oncology in South China, Collaborative Innovation Center for Cancer Medicine, Sun Yat-sen University Cancer Center, Guangzhou, China. [6]Department of Chemistry, Tsinghua-Peking Joint Center for Life Sciences, MOE Key Laboratory of Bioorganic Phosphorus Chemistry and Chemical Biology, Tsinghua University, Beijing, China. [7]GMU-GIBH Joint School of Life Sciences, Guangdong-Hong Kong-Macau Joint Laboratory for Cell Fate Regulation and Diseases, Guangzhou Medical University, Guangzhou, China. [8]Center for Research in Molecular Medicine and Chronic Diseases (CiMUS), Universidade de Santiago de Compostela (USC)-Instituto de Investigación Sanitaria, Santiago de Compostela, Spain. [9]Department of Anatomy and Developmental Biology, Monash University, Wellington Road, Clayton, Victoria, Australia. [10]Molecular Pathology Unit, Center for Cancer Research, Massachusetts General Hospital, Department of Pathology, Harvard Medical School, Boston, MA, USA; Gene Regulation Observatory, Broad Institute of MIT and Harvard, Cambridge, MA, USA. [11]Key Laboratory of Pesticide & Chemical Biology of Ministry of Education, Hubei Key Laboratory of Genetic Regulation and Integrative Biology, School of Life Sciences, Central China Normal University, Wuhan, China. [12]Guangzhou Key Laboratory of Formula-Pattern of Traditional Chinese Medicine, School of Traditional Chinese Medicine, Jinan University, Guangzhou, China. [13]These authors contributed equally: Shaoshuai Jiang, Xinyi Liu, Zhuheng Zhang, Mingzhu Yang. ✉e-mail: bj@xzhmu.edu.cn; fanlili@jnu.edu.cn; chiwei@mail.sysu.edu.cn; xiaoxuela@scu.edu.cn; dingjunj@mail.sysu.edu.cn

Methods

Animals

All animal procedures complied with the ethical guidelines of Sun Yat-sen University and were approved by the Institutional Animal Care and Use Committee (IACUC) of Sun Yat-sen University (Approval No. SYSU-IACUC-2022001881). Female C57BL/6 mice and male DBA/2 mice, purchased from the Laboratory Animal Center of Sun Yat-sen University, were mated to generate F1 BDF1 offspring. These BDF1 mice were used as embryo donors for microinjection experiments. The mice were housed under a 12 h light/12 h dark cycle.

Cell lines

J1 ES cells were used for JMJD2A ChIP–seq analysis, whereas *Jmjd2a/b/c*$^{fl/fl}$ (*Jmjd2*$^{fl/fl}$) ES cells[22,53] were employed for LoopID, TurboID, HiChIP, absolute quantification of chromatin architecture (AQuA)-HiChIP, Micro-C, ChIP–seq, cleavage under targets & tagmentation (Cut&Tag), Repli-seq and RNA-seq experiments. HEK293T cells served as the packaging system for lentivirus production. Neural stem-cell-derived preinduced pluripotent stem cells were used for de novo construction of E-P interactions to validate LoopID's chromatin-interaction-based labeling. To validate JMJD2 condensates, IF of JMJD2 was performed in additional three cell types: neural progenitor cells, human induced pluripotent stem cells and MCF7 breast cancer cells. To investigate JMJD2 condensate function during the ES cell-to-2CLC transition, we established two reporter systems: ZSCAN4-GFP::MEERVL-tdTomato and MERVL-GFP ES cell lines.

Microbe strains

Standard molecular cloning procedures were performed using *Escherichia coli* TOP10 and DH5α cells. For recombinant protein expression, we used BL21(DE3) *E. coli* cells.

Antibodies

The following antibodies were used: Alexa Fluor 488 (Thermo Fisher Scientific, cat. no. A-11008, RRID: AB_143165), Alexa Fluor 568 (Thermo Fisher Scientific, cat. no. A-11011, RRID: AB_143157), Alexa Fluor Plus 555 (Thermo Fisher Scientific, cat. no. A32932, RRID: AB_2762844), BRD4 (Abcam, cat. no. ab128874, RRID: AB_11145462), BRD4 (Abcam, cat. no. ab244221, AB_3677728), CDX2 (Abcam, cat. no. ab76541, RRID: AB_1523334), Flag (Sigma-Aldrich, cat. no. F1804, RRID: AB_262044), GFP (Proteintech, cat. no. 66002-1-IG, RRID: AB_11182611), H3 (Active Motif, cat. no. 39064, RRID: AB_3678651), H3K27ac (Abcam, cat. no. ab4729, RRID: AB_2118291), H3K4me3 (Abcam, cat. no. ab8580, RRID: AB_306649), H3K9me1 (Active Motif, cat. no. 39888, RRID: AB_3678652), H3K9me2 (Abcam, cat. no. ab1220, RRID: AB_449854), H3K9me3 (Abcam, cat. no. ab8898, RRID: AB_306848), H3K36me2 (Active Motif, cat. no. 39256, RRID: AB_3678653), H3K36me3 (Active Motif, cat. no. 61902, RRID: AB_3678650), HA (Abcam, cat. no. ab9110, RRID: AB_307019), HA (Proteintech, cat. no. 51064-2-AP, RRID: AB_11042321), HA (Cell Signaling Technology, cat. no. 3724, RRID: AB_1549585), JMJD2A (Bethyl, cat. no. A300-861A, RRID: AB_609461), JMJD2A (Santa Cruz Biotechnology, cat. no. sc-271210, RRID: AB_10610785), JMJD2B (Bethyl, cat. no. A301-478A, RRID: AB_999594), JMJD2B (Santa Cruz Biotechnology, cat. no. sc-374241, RRID: AB_10989205), JMJD2C (Novus, cat. no. NBP1-49600, RRID: AB_10011699), JMJD2C (Santa Cruz Biotechnology, cat. no. sc-515767, RRID: AB_3068588), mCherry (Abcam, cat. no. ab205402, RRID: AB_2722769), MED1 (Abcam, cat. no. ab64965, RRID: AB_1142301), NIPBL (Invitrogen, PA5-59316, RRID: AB_2640507), Normal Mouse IgG (Millipore, cat. no. 12-371, RRID: AB_145840), normal rabbit IgG (Millipore, cat. no. 12-370, RRID: AB_145841), OCT4 (Santa Cruz Biotechnology, cat. no. sc-5279, RRID: AB_628051), SadCas9 (Active Motif, cat. no. 61787, RRID: AB_2793766), SMC1A (Bethyl, cat. no. A300-055A, RRID: AB_2192467), SMC1A (Abcam, cat. no. ab21583, RRID: AB_2192477), SOX1 (Cell Signaling Technology, cat. no. 4194, RRID: AB_1904140), SpdCas9 (Active Motif, cat. no. 91123, RRID: AB_2793783), SpdCas9 (Active Motif, cat. no. 61957, RRID: AB_3068589), STAT3 (Cell Signaling Technology, cat. no. 12640S, RRID: AB_2629499), Tubulin (ABclonal, cat. no. AC008, RRID: AB_2773006), VIRMA (Cell Signaling Technology, cat. no. 88358S, RRID: AB_2800121), YY1 (Abcam, cat. no. ab109237, RRID: AB_10890662), YY1 (Santa Cruz Biotechnology, cat. no. sc-7341, RRID: AB_2257497).

LoopID

Cell preparation. The ES cell lines used for LoopID experiments were generated from *Jmjd2*$^{fl/fl}$ ES cells with expression of SadCas9-Tb(C) and SpdCas9-Tb(N). The sgRNAs targeting the E-P anchors of *Oct4* and *Nanog* were designed using CRISPick and expressed in these cell lines. We recommend designing a minimum of three sgRNAs for each anchor (that is, three for the enhancer and three for the promoter site). The cells were then incubated with biotin for 48 h to enable labeling.

Nuclear extract preparation. ES cells were expanded to 60 148-cm^2 dishes until they reached 80–90% confluence. The cells were then cross-linked with 2% (v/v) formaldehyde for 10 min, followed by quenching with 0.25 M glycine for 5 min. Cell lysis was performed twice using ice-cold Nonidet P-40 lysis buffer (10 mM Tris-HCl pH 7.5, 150 mM NaCl, 0.05% (v/v) Nonidet P-40) supplemented with freshly added 0.5 mM dithiothreitol, 0.2 mM phenylmethylsulfonyl fluoride and 1:1000 protease inhibitor cocktail (Sigma Mammalian Protease Inhibitor cocktail). The lysates were centrifuged at 20,000*g* for 10 min at 4 °C to pellet the nuclei, with the supernatant representing the cytoplasmic fraction.

Chromatin shearing. The nuclear pellets were washed twice with phosphate-buffered saline (PBS) with 1 mM EDTA and then gently resuspended in nuclear lysis buffer (50 mM Tris-HCl, 10 mM EDTA, 4% (wt/v) sodium dodecyl sulfate (SDS), pH 7.4) containing freshly added 1 mM dithiothreitol and protease inhibitor cocktail. After incubation for 10 min at room temperature, the nuclei were resuspended in 5 ml nuclear lysis buffer and mixed with 15 ml of 8 M urea buffer, followed by centrifugation at 16,100*g* for 25 min at room temperature. This washing step was repeated twice more. The chromatin pellets were then washed twice with 5 ml cell lysis buffer before being resuspended in sonication buffer (10 mM Tris-HCl pH 8.0, 100 mM NaCl, 1 mM EDTA, 0.5 mM EGTA, 0.1% (wt/v) Na-deoxycholate, 0.5% (wt/v) *N*-lauroylsarcosine) with freshly added protease inhibitors. Chromatin was sheared to 500–1000-bp fragments using a Branson Sonifier S-450 at 40% amplitude (three pulses of 1 s on/0.5 s off) in an ice-water bath. The sonicated chromatin was split into Eppendorf tubes and centrifuged at 20,000*g* for 10 min at 4 °C to collect the chromatins. The supernatant fractions were combined, and a portion was reverse cross-linked at 65 °C overnight to verify sonication efficiency.

Streptavidin enrichment. The chromatin samples were incubated overnight with 1 ml Dynabeads MyOne Streptavidin T1 (Invitrogen, 65602) in sonication buffer. The beads were washed four times with 15 ml sonication buffer and incubated for 10 min at 4 °C with rotation. The beads were then sequentially washed with: 0.1% (v/v) deoxycholate, 1% (v/v) Triton X-100, 1 mM EDTA, 50 mM HEPES (pH 7.5) and 500 mM NaCl, followed by 250 mM LiCl, 0.5% (v/v) NP-40, 0.5% (v/v) deoxycholate, 1 mM EDTA and 10 mM Tris-HCl (pH 8.1). For each wash step, the supernatant was completely removed, and the beads were transferred to a new tube. After the final wash, the sample was centrifuged at 20,000*g* for 1 min to remove any remaining supernatant, and as much supernatant as possible was carefully aspirated from the centrifuged beads. Then, 150 µl of 2× SDS sample buffer was added to the beads, followed by vortexing and heating at 95–100 °C for 5 min (with additional vortexing midway through heating). The sample was then vortexed again and allowed to cool to room temperature. The beads were separated using a magnet for 2–3 min, and the supernatant was

carefully transferred to a fresh LoBind microfuge tube. Next, 150 µl of 1× SDS sample buffer was added to the residual beads, followed by gentle vortexing and magnetic separation for 2–3 min. This eluate was pooled with the first collection in the LoBind tube. The beads were washed one more time with 100 µl of 1× SDS sample buffer and combined with the previous samples. After a final magnetic separation for 2–3 min, the entire sample was transferred into a fresh LoBind microfuge tube. At this point, samples could be flash-frozen in liquid N_2 and stored at −80 °C. The samples were then fractionated on by 10% SDS–PAGE, stained with GelCode Blue Safe Protein Stain (Thermo, 24596) and subjected to whole-lane liquid chromatography coupled with tandem mass spectrometry, followed by sequencing and data analysis. Mass spectrometry analysis was carried out on Orbitrap HFX and Orbitrap Fusion Lumos mass spectrometers (Thermo Fisher Scientific).

LoopID activity validation during cell cycle

To increase the proportion of M-phase cells, LoopID cell lines (with or without sgRNAs) were treated with 100 ng ml^{-1} nocodazole (Sigma-Aldrich, 487929) for 3 h. Cells were then harvested, cross-linked with 1% (v/v) formaldehyde at room temperature for 10 min and quenched with 0.125 M glycine for 5 min. Cell pellets were washed with PBS three times.

Before flow sorting, cell pellets were resuspended in PBS containing 0.1% (v/v) Triton X-100 and 2 mM EDTA for membrane permeabilization to facilitate antibody accessibility. After permeabilization, cells were resuspended in PBS containing 2% (wt/v) bovine serum albumin and 2 mM EDTA, and incubated with antibodies. Primary antibody incubations were performed for 1 h at room temperature using pMPM2 antibody (Merck Millipore, 05-368MG) to label mitotic chromosomes. Secondary antibody incubations were performed for 30 min at room temperature using APC-conjugated F(ab′)$_2$ fragment goat anti-mouse IgG (Thermo Fisher, 17-4010-82). After incubation with antibodies, cells were resuspended in PBS containing 20 ng ml^{-1} DAPI and filtered through 40-µm cell sieves before sorting.

Chromatin was extracted from sorted G1- and M-phase cells using a ChromaFlash Chromatin Extraction Kit (Epigentek, P-2001-100). The extracted chromatin was mixed with SDS–PAGE Protein Loading Buffer (Beyotime, P0015L), and the mixture was heated at 98 °C for 5 min for subsequent streptavidin-blot analysis.

Engineering E-P interactions

To engineer E-P interactions of two-cell-specific genes (Fig. 7), condensate-competent *JMJD2* fused with *SadCas9-ABI* or *SpdCas9-PYL* was introduced using site-specific sgRNAs to the enhancers and promoters, respectively, of *Zscan4* and *Nelfa* in ES cells with the *ZSCAN4-GFP::MERVL-tdTomato* double reporter. The cells were treated with 100 µM ABA (Sigma) for 96 h; then, the ABA was removed by changing the culture medium until 168 h. At 168 h, the cells were collected for detection of E-P interactions and gene expression. At 240 h, the cells were collected for fluorescence-activated cell sorting (FACS).

To demonstrate that proteins were efficiently biotinylated only when chromatin interactions were formed (Supplementary Fig. 1) we de novo constructed chromatin interactions using a chemically inducible system, following methods described in our previous work[43]. Briefly, CLOuD9 (System Biosciences) was fused with split-TurboID and then used to de novo construct the chromatin interactions induced by ABA. Two E-P interactions were de novo constructed, one involving *Dppa5a* in mouse embryonic fibroblasts and the other involving *Zscan4* in ES cells. The gRNAs for the E-P interaction of *Dppa5a* were employed per our prior published work[43], whereas those for the E-P interactions of *Zscan4* were based on sgRNAs shown in Fig. 7 in the present work. In brief, the two cell types were transfected with a piggyBac vector containing *spdCas9-PYL-TurboID(N)-puro* or *TurboID(C)-ABI-sadCas9-hygro*, respectively, then subjected to screening with 1 µg ml^{-1} puromycin and 300 µg ml^{-1} hygromycin for 5 days. After selection, cells containing the chemical-inducible LoopID systems and sgRNAs were treated with or without ABA to induce chromatin interactions. Simultaneously, biotin incubation was performed. Cells were harvested 48 h later, and streptavidin western blotting was conducted.

Cell culture

Jmjd2a$^{fl/fl}$/*b*$^{fl/fl}$/*c*$^{fl/fl}$:Rosa26::CreERT2 (*Jmjd2*$^{fl/fl}$) ES cells[22] and *Zscan4*-GFP::MERVL-tdTomato ES cells[47] were cultured as in a previous study. These cell lines were maintained in ES cell medium consisting of Dulbecco's modified Eagle medium (DMEM, high-glucose) supplemented with 15% (v/v) fetal bovine serum (FBS; Gibco), 1 mM sodium pyruvate (Gibco), 1 mM nonessential amino acids (Gibco), 1× GlutaMAX (Gibco), 0.1 mM β-mercaptoethanol (Gibco), 1,000 U ml^{-1} leukemia inhibitory factor and 2i inhibitors (1.5 µM CHIR99021 and 0.5 µM PD0325901). MERVL-GFP ES cells were cultured as in our previous study[54] in 2iL medium (1:1 DMEM/F12:neurobasal medium, 1% (v/v) N2 supplement, 2% (v/v) B27 supplement, 1× nonessential amino acids solution, 2 mM L-glutamine, 100 µg ml^{-1} L-ascorbic acid, 10 ng ml^{-1} LIF, 1 µM PD0325091, 3 µM CHIR99021, 110 µM 2-mercaptoethanol and primocin).

Neural progenitor cells were cultured in Neural Basal Medium (Gibco) supplemented with nonessential amino acids (Gibco), 0.5× GlutaMAX (Gibco), 1× B27 (Gibco), 1× N2 (Gibco), 0.075% (wt/v) bovine serum albumin (Sigma), 10 ng ml^{-1} bFGF (Peprotech) and 10 ng ml^{-1} mEGF (Peprotech). Human induced pluripotent stem cells were cultured in mTeSR medium (StemCell Technologies) on tissue culture plates coated with Matrigel (BD Bioscience). MCF7 cells were cultured in RPMI 1640 (Gibco) containing 10% (v/v) FBS (Lonsera). Mouse embryonic fibroblasts were cultured in DMEM supplemented with 10% (v/v) FBS and 100 U ml^{-1} penicillin–streptomycin (Gibco). All cells were cultured in 5% (v/v) CO_2 at 37 °C in an incubator.

Proteome data analysis

Looposome identification. SAINTexpress v.3.3 was used as a statistical tool to calculate a probability value for each potential protein compared to background contaminants using default parameters. Proteins with AvgP = 1 (FDR = 0), FC ≥ 3 versus −sgRNA and count ≥ 30 in both +sgRNA replicates were considered to be valid proteins.

Looposome classification. The detailed classification of looposome proteins was based on PANTHER Protein Class. The 'known' proteins in Fig. 1 refer to proteins identified by published H3K27ac or H3K4me3 ChIP–MS[19] or ChIP–seq[20]. Gene ontology analysis was performed using DAVID[55].

Differential analysis between looposomes. The differential analysis between looposomes was also performed with SAINTexpress using default parameters. Proteins that were enriched in at least one looposome, with FDR ≤ 0.05 and FC ≥ 1, were considered to be differential proteins.

Maintaining score. The maintaining score (Fig. 4a) was used to assess the correlation between the presence of a protein in the looposome and the condensate-forming ability of JMJD2. A higher score indicated a greater likelihood of the protein being retained within the looposome by JMJD2 condensates. The maintaining score was calculated as follows, and its significance was determined by averaging the differential significance of Mut-hIDR1 versus Mut, Ctrl versus TKO and Ctrl versus Mut, calculated by SAINTexpress:

$$\frac{\log_2[\mathrm{FC}]\left(\frac{\mathrm{Mut\_hIDR1}}{\mathrm{Mut}}\right)-\log_2[\mathrm{FC}]\left(\frac{\mathrm{hIDR1}}{\mathrm{Mut}}\right)}{0.5\times\left(\log_2[\mathrm{FC}]\left(\frac{\mathrm{Ctrl}}{\mathrm{TKO}}\right)+\log_2[\mathrm{FC}]\left(\frac{\mathrm{Ctrl}}{\mathrm{Mut}}\right)\right)}.$$

Immunoprecipitation coupled with mass spectrometry analysis. For the immunoprecipitation coupled with mass spectrometry results shown in Supplementary Fig. 3t, abundance of proteins was used as an input to SAINTexpress. Proteins with AvgP ≥ 0.8 were considered to be valid proteins.

Data presentation

Error bars represent the standard error of the mean. Box plots display the median as the center line, and the 25th and 75th percentiles as the bounds of the box; the whiskers represent the minimum and maximum values within 1.5 times the interquartile range from the lower and upper quartiles.

Statistics and reproducibility

LoopID was conducted with at least two replicates, and at least three replicates for −sgRNA groups. High-throughput chromatin conformation capture (Hi-C), HiChIP, Micro-C, circularized chromosome conformation capture combined with high-throughput sequencing (4C−seq), ChIP−seq, Cut&Tag and RNA-seq were conducted with at least two biological replicates, and coimmunoprecipitation, chromatin immunoprecipitation followed by PCR (ChIP−qPCR), chromosome conformation capture (3C), FACS, western blotting, IF, FISH, colony formation assay, and all imaging-related and cellular-phenotype-related experiments with at least three biological replicates. Numbers of independent repeats for other experiments are indicated in the figure legends. Representative experiments were repeated independently with similar results. All attempts at replication were successful. No statistical method was used to predetermine sample size, but the chosen sample sizes were consistent with those generally employed in the field and sufficient to support the conclusions of this study. Samples were randomly assigned to experimental groups, and data collection was performed in randomized order. The datasets, including puncta counts from imaging and ChIP−qPCR, PCR with reverse transcription, FACS, 3C−qPCR, HiChIP−qPCR and western blot data, closely followed a normal distribution, enabling use of parametric tests. Data collection and analysis were not performed blind to the conditions of the experiments. No data were excluded from the analyses.

Materials availability

DNA constructs and other research reagents generated by the authors will be distributed to other researchers on request to J.D. (dingjunj@mail.sysu.edu.cn).

Reporting summary

Further information on research design is available in the Nature Portfolio Reporting Summary linked to this article.

Data availability

All omics data generated in this study are summarized in Supplementary Table 8. HiChIP (mES cell H3K27ac), AQuA-HiChIP (H3K27ac), Micro-C (mES cell), 4C−seq (mES cell E-P loop of *Zscan4c*), ChIP−seq and Cut&Tag (mES cell H3K27ac, H3K36me3, H3K4me3, H3K9me2, H3K9me3, JMJD2A, JMJD2C, SadCas9, SpdCas9, YY1) are available through the Gene Expression Omnibus under accession GSE232848. The proteomics data generated in this study have been deposited in PRIDE under accession number PXD069064. Public ChIP−seq data from mES cells: BRD4 (Sabari et al.[7], GSE112808); CBX2, EZH2 and RING1B (Deaton et al.[56], GSE78899); CTCF, H3K27ac, H3K4me1 and H3K4me3 (Shen et al.[50], GSE29218); H3K27ac and p300 (Chronis et al.[57], GSE90893); H3K9me3 (Cho et al.[58], GSE106176); HDAC1, HDAC2 and LSD1 (Whyte et al.[59], GSE27841); HP1 and SMYD5 (Kidder et al.[60], GSE94033); JARID1B (Schmitz et al.[61], GSE31966); *Jmjd2a/b/c*-TKO (long-term) H3K9me3 (Pedersen et al.[22], GSE64254); JMJD2B and JMJD2C (Das et al.[36], GSE43231); JMJD3 (Banaszynski et al.[62], GSE42152); MLL2 and SUZ12 (Mas et al.[63], GSE99530); MLL3/4 (Dorighi et al.[64], GSE98063); MLL4 (Cao et al.[65], GSE99022); OCT4 (Whyte et al.[66], GSE44286); PRDM4 (Bogani et al.[67], GSE48372); SET1A (Sze et al.[68], GSE98988); SETDB1 (Bilodeau et al.[69], GSE18371); SUV39H1 and SUV39H2 (Bulut-Karslioglu et al.[70], GSE57092); TET1 (Williams et al.[71], GSE24841); YY1 (Weintraub et al.[9], GSE99518); USF1 and WDR5 (Scelfo et al.[72], GSE122715); UTX (Wang et al.[73], GSE103180). Public ChIP−seq data from two-cell embryos: H3K27ac and H3K4me3 (Dahl et al.[74], GSE72784). Public ChIP−seq data from 2CLCs: H3K27ac and H3K4me3 (Zhu et al.[46], GSE159623). Public 3D genome data from mES cells: H3K27ac HiChIP (Mumbach et al.[14], GSE101498); from two-cell embryos: Hi-C (Du et al.[75], GSE82185); from 2CLCs: Hi-C (Zhu et al.[46], GSE159623). Public RNA-seq data from from 2CLCs (Zhu et al.[46], GSE159623), ciTotiSCs (Hu et al.[76], GSE185000); mES cells, D-EPSCs and L-EPSCs (Posfai et al.[77], GSE145609); two-cell embryos (Zhang et al.[78], GSE71434); TLSCs (Yang et al.[54], GSE166204); bulk RNA-seq of mouse embryos (Wu et al.[79], GSE66390); and single-cell RNA-seq from mouse embryos (Fan et al.[80], GSE53386), totipotent blastomere-like cells (Shen et al.[81], GSE168728) and totipotent-like stem cells (Xu et al.[82], GSE183522). Source data are provided with this paper.

Code availability

Software and algorithms used in this study were as follows: scripts written in-house for this study (Calculation of maintaining score, https://github.com/XinyiLiu671/LoopID), 10X Genomics Cell Ranger v.7.1.0 (Zheng et al.[83], https://www.10xgenomics.com), Basic4Cseq v.1.38.0 (Walter et al.[84], https://bioconductor.org/packages/release/bioc/html/Basic4Cseq.html), bedtools v.2.26.0 (Quinlan et al.[85], https://github.com/arq5x/bedtools), BioGPS (Wu et al.[86], http://biogps.org/#goto=welcome), Bowtie2 v.2.3.0 (Langmead et al.[87], https://github.com/arq5x/bedtools), Cas-OFFinder (Bae et al.[88], http://www.rgenome.net/cas-offinder/), CRISPick (https://portals.broadinstitute.org/gppx/crispick/public), crisprScore v.1.10.0, (Hoberecht et al.[89], https://www.bioconductor.org/packages/release/bioc/html/crisprScore.html), Cytoscape v.3.9.1 (Shannon et al.[90], https://cytoscape.org), DAVID (Sherman et al.[55], https://david.ncifcrf.gov/tools.jsp), DeepTools v.3.5.1 (Ramírez et al.[91], https://deeptools.readthedocs.io/en/develop/content/list_of_tools.html), diffloop v.1.14.0 (Lareau et al.[92], http://bioconductor.org/packages/release/bioc/html/diffloop.html), EdgeR v.3.26.5 (Robinson et al.[93], https://bioconductor.org/packages/release/bioc/html/edgeR.html), Fastp v.0.23.2 (Chen et al.[94], https://github.com/OpenGene/fastp), FourCSeq v.1.2.0 (Klein et al.[95], https://bioconductor.riken.jp/packages/3.1/bioc/html/FourCSeq.html), GENOVA v.0.95 (van der Weide et al.[96], https://github.com/robinweide/GENOVA), ggplot2 v.3.4.3 (Wickham[97], https://ggplot2.tidyverse.org), ggpubr v.0.6.0 (Kassambara[98], https://cran.r-project.org/web/packages/ggpubr/index.html), GSEA v.4.0.3 (Subramanian et al.[99], https://www.gsea-msigdb.org/gsea/index.jsp), HiCExplore v.3.7.1 (Wolff et al.[100], https://hicexplorer.readthedocs.io/en/latest/index.html), hichipper v.0.7.5 (Lareau et al.[101], https://github.com/aryeelab/hichipper), HiC-Pro v.2.10.0 (Servant et al.[102], https://github.com/nservant/HiC-Pro), HOMER v.4.11 (Heinz et al.[103], http://homer.ucsd.edu/homer), HTSeq-count v.0.11.2 (Anders et al.[104], https://github.com/simon-anders/htseq), IGV v.2.4.10 (Thorvaldsdottir et al.[105], http://software.broadinstitute.org/software/igv), ImageJ (Schneider et al.[106], https://imagej.nih.gov), Imaris (Bitplane, https://imaris.oxinst.com), Juicebox v.1.9.8 (Robinson et al.[107], https://www.aidenlab.org/juicebox), Macs2 v.2.1.2 (Zhang et al.[108], https://github.com/taoliu/MACS), Mouse Reference Genome, NCBI build 37, NCBI37/mm9 (Genome Reference Consortium, https://www.ncbi.nlm.nih.gov/grc/mouse), PANTHER (Thomas et al.[109], https://www.pantherdb.org), Perl v.5.34.0 (Wall et al.[110], https://www.perl.org), SAINTexpress v.3.3 (Teo et al.[17], https://saint-apms.sourceforge.net/Main.html).

References

53. Pedersen, M. T. et al. The demethylase JMJD2C localizes to H3K4me3-positive transcription start sites and is dispensable for embryonic development. *Mol. Cell. Biol.* **34**, 1031–1045 (2014).
54. Yang, M. et al. Chemical-induced chromatin remodeling reprograms mouse ESCs to totipotent-like stem cells. *Cell Stem Cell* **29**, 400–418 (2022).
55. Sherman, B. T. et al. DAVID: a web server for functional enrichment analysis and functional annotation of gene lists (2021 update). *Nucleic Acids Res* **50**, W216–W221 (2022).
56. Deaton, A. M. et al. Enhancer regions show high histone H3.3 turnover that changes during differentiation. *eLife* **5**, e15316 (2016).
57. Chronis, C. et al. Cooperative binding of transcription factors orchestrates reprogramming. *Cell* **168**, 442–459 (2017).
58. Cho, S. W. et al. Promoter of lncRNA gene PVT1 is a tumor-suppressor DNA boundary element. *Cell* **173**, 1398–1412 (2018).
59. Whyte, W. A. et al. Enhancer decommissioning by LSD1 during embryonic stem cell differentiation. *Nature* **482**, 221–225 (2012).
60. Kidder, B. L. et al. SMYD5 regulates H4K20me3-marked heterochromatin to safeguard ES cell self-renewal and prevent spurious differentiation. *Epigenetics Chromatin* **10**, 8 (2017).
61. Schmitz, S. U. et al. Jarid1b targets genes regulating development and is involved in neural differentiation. *EMBO J.* **30**, 4586–4600 (2011).
62. Banaszynski, L. A. et al. Hira-dependent histone H3.3 deposition facilitates PRC2 recruitment at developmental loci in ES cells. *Cell* **155**, 107–120 (2013).
63. Mas, G. et al. Promoter bivalency favors an open chromatin architecture in embryonic stem cells. *Nat. Genet.* **50**, 1452–1462 (2018).
64. Dorighi, K. M. et al. Mll3 and Mll4 facilitate enhancer RNA synthesis and transcription from promoters independently of H3K4 monomethylation. *Mol. Cell* **66**, 568–576 (2017).
65. Cao, K. et al. An Mll4/COMPASS-Lsd1 epigenetic axis governs enhancer function and pluripotency transition in embryonic stem cells. *Sci. Adv.* **4**, eaap8747 (2018).
66. Whyte, W. A. et al. Master transcription factors and mediator establish super-enhancers at key cell identity genes. *Cell* **153**, 307–319 (2013).
67. Bogani, D. et al. The PR/SET domain zinc finger protein Prdm4 regulates gene expression in embryonic stem cells but plays a nonessential role in the developing mouse embryo. *Mol. Cell. Biol.* **33**, 3936–3950 (2013).
68. Sze, C. C. et al. Histone H3K4 methylation-dependent and -independent functions of Set1A/COMPASS in embryonic stem cell self-renewal and differentiation. *Genes Dev.* **31**, 1732–1737 (2017).
69. Bilodeau, S. et al. SetDB1 contributes to repression of genes encoding developmental regulators and maintenance of ES cell state. *Genes Dev.* **23**, 2484–2489 (2009).
70. Bulut-Karslioglu, A. et al. Suv39h-dependent H3K9me3 marks intact retrotransposons and silences LINE elements in mouse embryonic stem cells. *Mol. Cell* **55**, 277–290 (2014).
71. Williams, K. et al. TET1 and hydroxymethylcytosine in transcription and DNA methylation fidelity. *Nature* **473**, 343–348 (2011).
72. Scelfo, A. et al. Functional landscape of PCGF proteins reveals both RING1A/B-dependent-and RING1A/B-independent-specific activities. *Mol. Cell* **74**, 1037–1052 (2019).
73. Wang, A. H. et al. The elongation factor Spt6 maintains ESC pluripotency by controlling super-enhancers and counteracting Polycomb proteins. *Mol. Cell* **68**, 398–413 (2017).
74. Dahl, J. A. et al. Broad histone H3K4me3 domains in mouse oocytes modulate maternal-to-zygotic transition. *Nature* **537**, 548–552 (2016).
75. Du, Z. et al. Allelic reprogramming of 3D chromatin architecture during early mammalian development. *Nature* **547**, 232–235 (2017).
76. Hu, Y. et al. Induction of mouse totipotent stem cells by a defined chemical cocktail. *Nature* **617**, 792–797 (2023).
77. Posfai, E. et al. Evaluating totipotency using criteria of increasing stringency. *Nat. Cell Biol.* **23**, 49–60 (2021).
78. Zhang, B. et al. Allelic reprogramming of the histone modification H3K4me3 in early mammalian development. *Nature* **537**, 553–557 (2016).
79. Wu, J. et al. The landscape of accessible chromatin in mammalian preimplantation embryos. *Nature* **534**, 652–657 (2016).
80. Fan, X. et al. Single-cell RNA-seq transcriptome analysis of linear and circular RNAs in mouse preimplantation embryos. *Genome Biol.* **16**, 148 (2015).
81. Shen, H. et al. Mouse totipotent stem cells captured and maintained through spliceosomal repression. *Cell* **184**, 2843–2859 (2021).
82. Xu, Y. et al. Derivation of totipotent-like stem cells with blastocyst-like structure forming potential. *Cell Res.* **32**, 513–529 (2022).
83. Zheng, G. X. et al. Massively parallel digital transcriptional profiling of single cells. *Nat. Commun.* **8**, 14049 (2017).
84. Walter, C. et al. Basic4Cseq: an R/Bioconductor package for analyzing 4C-seq data. *Bioinformatics* **30**, 3268–3269 (2014).
85. Quinlan, A. R. et al. BEDTools: a flexible suite of utilities for comparing genomic features. *Bioinformatics* **26**, 841–842 (2010).
86. Wu, C. et al. BioGPS: an extensible and customizable portal for querying and organizing gene annotation resources. *Genome Biol.* **10**, R130 (2009).
87. Langmead, B. et al. Fast gapped-read alignment with Bowtie 2. *Nat. Methods* **9**, 357–359 (2012).
88. Bae, S. et al. Cas-OFFinder: a fast and versatile algorithm that searches for potential off-target sites of Cas9 RNA-guided endonucleases. *Bioinformatics* **30**, 1473–1475 (2014).
89. Hoberecht, L. et al. A comprehensive Bioconductor ecosystem for the design of CRISPR guide RNAs across nucleases and technologies. *Nat. Commun.* **13**, 6568 (2022).
90. Shannon, P. et al. Cytoscape: a software environment for integrated models of biomolecular interaction networks. *Genome Res.* **13**, 2498–2504 (2003).
91. Ramírez, F. et al. deepTools2: a next generation web server for deep-sequencing data analysis. *Nucleic Acids Res.* **44**, W160–W165 (2016).
92. Lareau, C. A. et al. diffloop: a computational framework for identifying and analyzing differential DNA loops from sequencing data. *Bioinformatics* **34**, 672–674 (2018).
93. Robinson, M. D. et al. edgeR: a Bioconductor package for differential expression analysis of digital gene expression data. *Bioinformatics* **26**, 139–140 (2010).
94. Chen, S. et al. fastp: an ultra-fast all-in-one FASTQ preprocessor. *Bioinformatics* **34**, i884–i890 (2018).
95. Klein, F. A. et al. FourCSeq: analysis of 4C sequencing data. *Bioinformatics* **31**, 3085–3091 (2015).
96. van der Weide, R. H. et al. Hi-C analyses with GENOVA: a case study with cohesin variants. *NAR Genom. Bioinform.* **3**, lqab040 (2021).
97. Wickham, H. *ggplot2: Elegant Graphics for Data Analysis* (Springer-Verlag, 2016).
98. Kassambara, A. ggpubr: 'ggplot2' based publication ready plots. https://cran.r-project.org/web/packages/ggpubr/index.html (2023).
99. Subramanian, A. et al. Gene set enrichment analysis: a knowledge-based approach for interpreting genome-wide expression profiles. *Proc. Natl Acad. Sci. USA* **102**, 15545–15550 (2005).

100. Wolff, J. et al. Galaxy HiCExplorer 3: a web server for reproducible Hi-C, capture Hi-C and single-cell Hi-C data analysis, quality control and visualization. *Nucleic Acids Res.* **48**, W177–W184 (2020).
101. Lareau, C. A. et al. hichipper: a preprocessing pipeline for calling DNA loops from HiChIP data. *Nat. Methods* **15**, 155–156 (2018).
102. Servant, N. et al. HiC-Pro: an optimized and flexible pipeline for Hi-C data processing. *Genome Biol.* **16**, 259 (2015).
103. Heinz, S. et al. Simple combinations of lineage-determining transcription factors prime *cis*-regulatory elements required for macrophage and B cell identities. *Mol. Cell* **38**, 576–589 (2010).
104. Anders, S. et al. HTSeq–a Python framework to work with high-throughput sequencing data. *Bioinformatics* **31**, 166–169 (2015).
105. Thorvaldsdottir, H. et al. Integrative Genomics Viewer (IGV): high-performance genomics data visualization and exploration. *Brief. Bioinform.* **14**, 178–192 (2013).
106. Schneider, C. A. et al. NIH Image to ImageJ: 25 years of image analysis. *Nat. Methods* **9**, 671–675 (2012).
107. Robinson, J. T. et al. Juicebox.js provides a cloud-based visualization system for Hi-C data. *Cell Syst.* **6**, 256–258 (2018).
108. Zhang, Y. et al. Model-based analysis of ChIP-Seq (MACS). *Genome Biol.* **9**, R137 (2008).
109. Thomas, P. D. et al. PANTHER: making genome-scale phylogenetics accessible to all. *Protein Sci.* **31**, 8–22 (2022).
110. Wall, L., Christiansen, T. & Orwant, J. *Programming Perl* (O'Reilly Media, 2000).

Acknowledgements

We thank K. Helin and K. Agger (University of Copenhagen, Denmark) for help with JMJD2 cell lines, and R. A. Young (Whitehead Institute for Biomedical Research, USA) for pET-mEGFP plasmids. This work was funded by the National Key Research and Development Program of China (2023YFA1800900) (J.J.D.); National Key Research and Development Program of China (2024YFA1106900) (J.J.D.); National Science Foundation for Distinguished Young Scholars of China (32425022) (J.J.D.); National Natural Science Foundation of China (32170798 and 32430031) (J.J.D.); Guangdong Innovative and Entrepreneurial Research Team Program (2016ZT06S029) (J.J.D.); National Natural Science Foundation of China (32300669) (S.S.J.); Sun Yat-sen University Fundamental Research Funds for Colleges and Universities Young Teachers Cultivation Project (23ptpy89) (S.S.J.); Natural Science Foundation of Guangdong Province (2024A1515011174) (S.S.J.); National Natural Science Foundation of China (32400659) (X.Y.L.); China Postdoctoral Science Foundation (2023M744082) (X.Y.L.); Natural Science Foundation of Guangdong Province (2023A1515010148) (J.S.); National Natural Science Foundation of China (32400561) (J.S.); Guangdong Basic and Applied Basic Research Foundation (2025B1515020011) (L.L.F.); Guangzhou Science and Technology Program Project, China (No.2025A04J5154) (L.L.F.); National Natural Science Foundation of China (82304746) (L.L.F.); National Natural Science Foundation of China (323B2026) (J.L.Q.); and NIH/NHGRI (1R35HG010717-01) (L.P.); Rappaport MGH Research Scholar Award 2024-2029 (L.P.).

Author contributions

S.J., X.L. and J.D. designed the study; S.J., X.L. and J.D. discussed the results and wrote the manuscript with input from all other authors; X.L. performed bioinformatic analyses and visualizations; X.H., J.T., Z. Zhang. and L.M. conducted experiments on biomolecular condensates; X.Z., X.L., H. Lin., X.H. and Z. Zhang performed the LoopID, HiChIP and ChIP experiments; Q.T., Z.W., Z. Zhou, L.Z., H. Li. and J.Q. constructed plasmids and performed transfections; P.P.D. and L.P. provided the ChIP–seq data for JMJD2A and KDM4A; J.L. and Z.D. prepared nucleosome arrays modified with H3K4me3; M.Y. generated the chimeras; and J.S., J.W., H.W., D.-f.H., J.B., L.F., W.C., X.X., J.C.W., D.G. and L.W. provided guidance for the manuscript.

Competing interests

The authors declare no competing interests.

Additional information

Supplementary information The online version contains supplementary material available at https://doi.org/10.1038/s41588-025-02415-8.

Correspondence and requests for materials should be addressed to Jin Bai, Lili Fan, Wei Chi, Xue Xiao or Junjun Ding.

Peer review information *Nature Genetics* thanks Alessio Zippo and the other, anonymous, reviewer(s) for their contribution to the peer review of this work. Peer reviewer reports are available.

nature portfolio

Corresponding author(s): Junjun Ding

Last updated by author(s): Mar 31, 2025

Reporting Summary

Nature Portfolio wishes to improve the reproducibility of the work that we publish. This form provides structure for consistency and transparency in reporting. For further information on Nature Portfolio policies, see our Editorial Policies and the Editorial Policy Checklist.

Statistics

For all statistical analyses, confirm that the following items are present in the figure legend, table legend, main text, or Methods section.

n/a	Confirmed
☐	☒ The exact sample size (*n*) for each experimental group/condition, given as a discrete number and unit of measurement
☐	☒ A statement on whether measurements were taken from distinct samples or whether the same sample was measured repeatedly
☐	☒ The statistical test(s) used AND whether they are one- or two-sided *Only common tests should be described solely by name; describe more complex techniques in the Methods section.*
☒	☐ A description of all covariates tested
☐	☒ A description of any assumptions or corrections, such as tests of normality and adjustment for multiple comparisons
☐	☒ A full description of the statistical parameters including central tendency (e.g. means) or other basic estimates (e.g. regression coefficient) AND variation (e.g. standard deviation) or associated estimates of uncertainty (e.g. confidence intervals)
☐	☒ For null hypothesis testing, the test statistic (e.g. *F*, *t*, *r*) with confidence intervals, effect sizes, degrees of freedom and *P* value noted *Give P values as exact values whenever suitable.*
☒	☐ For Bayesian analysis, information on the choice of priors and Markov chain Monte Carlo settings
☒	☐ For hierarchical and complex designs, identification of the appropriate level for tests and full reporting of outcomes
☐	☒ Estimates of effect sizes (e.g. Cohen's *d*, Pearson's *r*), indicating how they were calculated

Our web collection on statistics for biologists contains articles on many of the points above.

Software and code

Policy information about availability of computer code

Data collection	No software was used for data collection.
Data analysis	Detailed in the "Code availability" in the Methods section: 10X Genomics Cell Ranger v7.1.0 Basic4Cseq v1.38.0 Bedtools v2.26.0 Bowtie2 v2.3.0 Cas-OFFinder CRISPick crisprScore v1.10.0 Cytoscape v3.9.1 DAVID DeepTools v3.5.1 Diffloop v1.14.0 EdgeR v3.26.5 Fastp v0.23.2 FourCSeq v1.2.0 GENOVA v0.95 Ggplot2 v3.4.3 Ggpubr v0.6.0 GSEA v4.0.3

HiCExplore v3.7.1
Hichipper v0.7.5
HiC-Pro v2.10.0
Homemade scripts: https://github.com/XinyiLiu671/LoopID
HOMER v4.11
HTSeq-count v0.11.2
Igv v2.4.10
ImageJ
Imaris
Juicebox v1.9.8
Macs2 v2.1.2
Mouse reference genome, NCBI build 37
PANTHER
Perl v5.34.0
SAINTexpress v3.3

For manuscripts utilizing custom algorithms or software that are central to the research but not yet described in published literature, software must be made available to editors and reviewers. We strongly encourage code deposition in a community repository (e.g. GitHub). See the Nature Portfolio guidelines for submitting code & software for further information.

Data

Policy information about availability of data

All manuscripts must include a data availability statement. This statement should provide the following information, where applicable:

- Accession codes, unique identifiers, or web links for publicly available datasets
- A description of any restrictions on data availability
- For clinical datasets or third party data, please ensure that the statement adheres to our policy

Data produced by this study: GSE232848

Other data, detailed in the "Data availability" in the Methods section:
Public ChIP-seq data. Data from mESCs: BRD4 (Sabari et al., GSE112808), CBX2, EZH2 and RING1B (Deaton et al., GSE78899), CTCF, H3K27ac, H3K4me1 and H3K4me3 (Shen et al., GSE29218), H3K27ac and p300 (Chronis et al., GSE90893), H3K9me3 (Cho et al., GSE106176), HDAC1, HDAC2 and LSD1 (Whyte et al., GSE27841), HP1 and SMYD5 (Kidder et al., GSE94033), JARID1B (Schmitz et al., GSE31966), Jmjd2a/b/c-TKO (long-term) H3K9me3 (Pedersen et al., GSE64254), JMJD2B and JMJD2C (Das et al., GSE43231), JMJD3 (Banaszynski et al., GSE42152), MLL2 and SUZ12 (Mas et al., GSE99530), MLL3/4 (Dorighi et al., GSE98063), MLL4 (Cao et al., GSE99022), OCT4 (Whyte et al., GSE44286), PRDM4 (Bogani et al., GSE48372), SET1A (Sze et al., GSE98988), SETDB1 (Bilodeau et al., GSE18371), SUV39H1 and SUV39H2 (Bulut-Karslioglu et al., GSE57092), TET1 (Williams et al., GSE24841), YY1 (Weintraub et al., GSE99518), USF1 and WDR5 (Scelfo et al., GSE122715), UTX (Wang et al., GSE103180). Data from 2-cell embryos: H3K27ac and H3K4me3 (Dahl et al., GSE72784). Data from 2CLCs: H3K27ac and H3K4me3 (Zhu et al., GSE159623).
Public 3D genome data. Data from mESCs: H3K27ac HiChIP (Mumbach et al., GSE101498). Data from 2-cell embryos: Hi-C (Du et al., GSE82185). Data from 2CLCs: Hi-C (Zhu et al., GSE159623).
Public RNA-seq data. Data from 2CLCs (Zhu et al., GSE159623), ciTotiSCs (Hu et al., GSE185000), mESCs, D-EPSCs and L-EPSCs (Posfai et al., GSE145609), 2-cell embryos (Zhang et al., GSE71434), TLSCs (Yang et al., GSE166204), bulk RNA-seq of mouse embryos (Wu et al., GSE66390), single-cell RNA-seq of mouse embryos (Fan et al., GSE53386), TBLCs (Shen et al., GSE168728), and TPSCs (Xu et al., GSE183522).

Research involving human participants, their data, or biological material

Policy information about studies with human participants or human data. See also policy information about sex, gender (identity/presentation), and sexual orientation and race, ethnicity and racism.

Reporting on sex and gender	N/A
Reporting on race, ethnicity, or other socially relevant groupings	N/A
Population characteristics	N/A
Recruitment	N/A
Ethics oversight	N/A

Note that full information on the approval of the study protocol must also be provided in the manuscript.

Field-specific reporting

Please select the one below that is the best fit for your research. If you are not sure, read the appropriate sections before making your selection.

☒ Life sciences ☐ Behavioural & social sciences ☐ Ecological, evolutionary & environmental sciences

For a reference copy of the document with all sections, see nature.com/documents/nr-reporting-summary-flat.pdf

Life sciences study design

All studies must disclose on these points even when the disclosure is negative.

Sample size	Experiments were performed on cell lines. LoopID (with at least 2 replicates, and at least 3 replicates for '-sgRNA' groups), Hi-C, HiChIP, Micro-C, 4C-seq, ChIP-seq, Cut & Tag, and RNA-seq were conducted with at least 2 biological replicates, whereas ChIP-qPCR, 3C, FACS, Western blotting, colony formation assay, and imaging were conducted with at least 3 biological replicates. No statistical method was used to predetermine sample size, but the chosen sample sizes are consistent with those generally employed in the field and sufficient to support the conclusions of this study.
Data exclusions	No data were excluded from analyses.
Replication	LoopID (with at least 2 replicates, and at least 3 replicates for '-sgRNA' groups), Hi-C, HiChIP, Micro-C, 4C-seq, ChIP-seq, Cut & Tag, and RNA-seq were conducted with at least 2 biological replicates, whereas ChIP-qPCR, 3C, FACS, Western blotting, colony formation assay, and imaging were conducted with at least 3 biological replicates. All attempts at replication were successful.
Randomization	Samples were randomly assigned to experimental groups, and data collection was performed in a randomized order.
Blinding	Data collection and analysis were not performed blind to the conditions of the experiments.

Reporting for specific materials, systems and methods

We require information from authors about some types of materials, experimental systems and methods used in many studies. Here, indicate whether each material, system or method listed is relevant to your study. If you are not sure if a list item applies to your research, read the appropriate section before selecting a response.

Materials & experimental systems

n/a	Involved in the study
☐	☒ Antibodies
☐	☒ Eukaryotic cell lines
☒	☐ Palaeontology and archaeology
☐	☒ Animals and other organisms
☒	☐ Clinical data
☒	☐ Dual use research of concern
☒	☐ Plants

Methods

n/a	Involved in the study
☐	☒ ChIP-seq
☐	☒ Flow cytometry
☒	☐ MRI-based neuroimaging

Antibodies

Antibodies used	Alexa Fluor 488 (Thermo Fisher Scientific, Cat# A-11008, RRID:AB_143165), Alexa Fluor 568 (Thermo Fisher Scientific, Cat# A-11011, RRID:AB_143157), Alexa Fluor™ Plus 555 (Thermo Fisher Scientific, Cat# A32932, RRID:AB_2762844), BRD4 (Abcam, Cat# ab128874, RRID:AB_11145462), BRD4 (Abcam, Cat# ab244221, AB_3677728), CDX2 (Abcam, Cat# ab76541, RRID:AB_1523334), FLAG (Sigma-Aldrich, Cat# F1804, RRID:AB_262044), GFP (Proteintech, Cat# 66002-1-IG, RRID:AB_11182611), H3 (Active Motif, Cat# 39064, RRID: AB_3678651), H3K27ac (Abcam, Cat# ab4729, RRID:AB_2118291), H3K4me3 (Abcam, Cat# ab8580, RRID:AB_306649), H3K9me1 (Active Motif, Cat# 39888, RRID: AB_3678652), H3K9me2 (Abcam, Cat# ab1220, RRID:AB_449854), H3K9me3 (Abcam, Cat# ab8898, RRID:AB_306848), H3K36me2 (Active Motif, Cat# 39256, RRID: AB_3678653), H3K36me3 (Active Motif, Cat# 61902, RRID: AB_3678650), HA (Abcam, Cat# ab9110, RRID:AB_307019), HA (Proteintech, Cat# 51064-2-AP, RRID:AB_11042321), HA (Cell Signaling Technology, Cat# 3724, RRID:AB_1549585), JMJD2A (Bethyl, Cat# A300-861A, RRID:AB_609461), JMJD2A (Santa Cruz Biotechnology, Cat# sc-271210, RRID:AB_10610785), JMJD2B (Bethyl, Cat# A301-478A, RRID:AB_999594), JMJD2B (Santa Cruz Biotechnology, Cat# sc-374241, RRID:AB_10989205), JMJD2C (Novus, Cat# NBP1-49600, RRID:AB_10011699), JMJD2C (Santa Cruz Biotechnology, Cat# sc-515767, RRID:AB_3068588), mCherry (Abcam, Cat# ab205402, RRID:AB_2722769), MED1 (Abcam, Cat# ab64965, RRID:AB_1142301), NIPBL (Invitrogen, PA5-59316, RRID:AB_2640507), Normal Mouse IgG (Millipore, Cat# 12-371, RRID:AB_145840), Normal Rabbit IgG (Millipore, Cat# 12-370, RRID:AB_145841), OCT4 (Santa Cruz Biotechnology, Cat# sc-5279, RRID:AB_628051), SadCas9 (Active Motif, Cat# 61787, RRID:AB_2793766), SMC1A (Bethyl, Cat# A300-055A, RRID:AB_2192467), SMC1A (Abcam, Cat# ab21583, RRID:AB_2192477), SOX1 (Cell Signaling Technology, Cat# 4194, RRID:AB_1904140), SpdCas9 (Active Motif, Cat# 91123, RRID:AB_2793783), SpdCas9 (Active Motif, Cat# 61957, RRID:AB_3068589), STAT3 (Cell Signaling Technology, Cat# 12640S, RRID:AB_2629499), TUBULIN (ABclonal, Cat# AC008, RRID:AB_2773006), VIRMA (Cell Signaling Technology, Cat# 88358S, RRID:AB_2800121), YY1 (Abcam, Cat# ab109237, RRID:AB_10890662), YY1 (Santa Cruz Biotechnology, Cat# sc-7341, RRID:AB_2257497).
Validation	All antibodies used in this study can be accessed via their respective RRIDs.

Eukaryotic cell lines

Policy information about cell lines and Sex and Gender in Research

Cell line source(s)	J1 embryonic stem cells (ESCs) were used for JMJD2A ChIP-seq analysis, while Jmjd2a/b/cfl/fl ESCs were employed for

Cell line source(s)	LoopID, TurboID, HiChIP, AQuA-HiChIP, Micro-C, ChIP-seq, Cut & Tag, Repli-seq and RNA-seq experiments. HEK293T cells served as the packaging system for lentivirus production. Neural stem cell-derived pre-induced pluripotent stem cells (NS-pre-iPSCs) were utilized for de novo construction of E-P interactions to validate LoopID's chromatin interaction-based labeling. To validate JMJD2 condensates, immunofluorescence (IF) of JMJD2 was performed in additional three cell types: neural progenitor cells (NPCs), induced pluripotent stem cells (hiPSCs), and MCF7 breast cancer cells. To investigate JMJD2 condensate function during the ESC-to-2-cell-like cell (2CLC) transition, we established two reporter systems: ZSCAN4-GFP::MEERVL-tdTomato and MERVL-GFP ESC lines.
Authentication	The J1 mESCs and the HEK293T cells were kindly provided by Dr. Jianlong Wang (PMID: 25936917). The Jmjd2a/b/c^fl/fl ESCs were obtained from PMID: 27266524. The NS-pre-iPSCs were from PMID: 18942890, and the hiPSCs were from PMID: 30405129. The NPCs were differentiated from the Jmjd2a/b/c^fl/fl ESCs following a published protocol (PMID: 12524553). The MCF7 cell line was kindly provided by Dr. Hai Hu (PMID: 26824656). The ZSCAN4-GFP::MEERVL-tdTomato reporter ESC line was obtained from PMID: 32032525, and the MERVL-GFP reporter ESC line was from PMID: 35143761.
Mycoplasma contamination	All cell lines tested negative for mycoplasma contamination.
Commonly misidentified lines (See ICLAC register)	No commonly misidentified cell lines were used.

Animals and other research organisms

Policy information about studies involving animals; ARRIVE guidelines recommended for reporting animal research, and Sex and Gender in Research

Laboratory animals	Female C57BL/6 mice and male DBA/2 mice, purchased from the Laboratory Animal Center of Sun Yat-sen University, were mated to generate F1 BDF1 offspring. These BDF1 mice were used as embryo donors for microinjection experiments. The mice were housed under a 12h light/12h dark cycle.
Wild animals	N/A
Reporting on sex	N/A
Field-collected samples	N/A
Ethics oversight	All animal procedures complied with the ethical guidelines of Sun Yat-sen University and were approved by the Institutional Animal Care and Use Committee (IACUC) of Sun Yat-sen University (Approval No. SYSU-IACUC-2022001881).

Note that full information on the approval of the study protocol must also be provided in the manuscript.

Plants

Seed stocks	N/A
Novel plant genotypes	N/A
Authentication	N/A

ChIP-seq

Data deposition

☒ Confirm that both raw and final processed data have been deposited in a public database such as GEO.

☒ Confirm that you have deposited or provided access to graph files (e.g. BED files) for the called peaks.

Data access links *May remain private before publication.*	Data produced by this study: GSE232848
Files in database submission	bigWig files with bin size of 10bp normalized by RPKM from ChIP-seq data for viewing in a genome browser.
Genome browser session (e.g. UCSC)	N/A

Methodology

Replicates	All ChIP-seq or other profiling experiment were performed on two biological replicates. The biological replicates were two independent differentiation experiments.
Sequencing depth	The ChIP-seq data were paired-end 150bp reads, with at least 7 GB per replicate.
Antibodies	Antibodies used for ChIP-seq or Cut & Tag include: FLAG (Sigma-Aldrich, Cat# F1804, RRID:AB_262044), H3K27ac (Abcam, Cat# ab4729, RRID:AB_2118291), H3K4me3 (Abcam, Cat# ab8580, RRID:AB_306649), H3K9me2 (Abcam, Cat# ab1220, RRID:AB_449854), H3K9me3 (Abcam, Cat# ab8898, RRID:AB_306848), H3K36me3 (Active Motif, Cat# 61902, RRID: AB_3678650), JMJD2A (Bethyl, Cat# A300-861A, RRID:AB_609461), JMJD2C (Santa Cruz Biotechnology, Cat# sc-515767, RRID:AB_3068588), SadCas9 (Active Motif, Cat# 61787, RRID:AB_2793766), SpdCas9 (Active Motif, Cat# 61957, RRID:AB_3068589), and YY1 (Abcam, Cat# ab109237, RRID:AB_10890662).
Peak calling parameters	Macs2 was used for peak calling with the default parameters (macs2 callpeak -g mm -q 0.05 -m 5 50).
Data quality	Sufficient sequencing depth was achieved according to ENCODE standards, with each replicate containing about 30 million usable fragments. The number of called peaks was compared to published data and was found to be quite comparable.
Software	Detailed in the "Code availability" in the Methods section: Bedtools v2.26.0 Bowtie2 v2.3.0 DeepTools v3.5.1 Fastp v0.23.2 HOMER v4.11 Igv v2.4.10 Macs2 v2.1.2 Mouse reference genome, NCBI build 37

Flow Cytometry

Plots

Confirm that:

☒ The axis labels state the marker and fluorochrome used (e.g. CD4-FITC).

☒ The axis scales are clearly visible. Include numbers along axes only for bottom left plot of group (a 'group' is an analysis of identical markers).

☒ All plots are contour plots with outliers or pseudocolor plots.

☒ A numerical value for number of cells or percentage (with statistics) is provided.

Methodology

Sample preparation	Single-cell suspensions were prepared and fixed, with at least 5×10^4 cells used per experiment.
Instrument	CytoFLEX
Software	The results were analyzed using FlowJo software.
Cell population abundance	At least 5x10^4 cells per experiment.
Gating strategy	Wild-type mES cells or mES cells transfected with an empty vector were used as negative controls.

☒ Tick this box to confirm that a figure exemplifying the gating strategy is provided in the Supplementary Information.